J. Fluid Mech. (1979), *vol.* 94, *part* 2, *pp.* 275–304
Printed in Great Britain

Stability and mixing of a vertical plane buoyant jet in confined depth

By GERHARD H. JIRKA
School of Civil and Environmental Engineering, Cornell University, Ithaca, New York
AND DONALD R. F. HARLEMAN
Department of Civil Engineering, Massachusetts Institute of Technology, Cambridge

(Received 3 October 1978)

A plane turbulent buoyant jet discharging vertically into a two-dimensional channel of confined depth is considered. The channel opens at both ends into a large outside reservoir, thus defining a steady symmetrical flow field within the channel. The analysis is aimed at two aspects, the stability and the bulk mixing characteristics of the discharge. A stable discharge configuration is defined as one in which a buoyant surface layer is formed which spreads horizontally and does not communicate with the initial buoyant jet region. On the other hand, the discharge configuration is unstable when a recirculating cell exists on both sides of the jet efflux.

It is shown that discharge stability is only dependent on the dynamic interaction of three near-field regions, a buoyant jet region, a surface impingement region and an internal hydraulic jump region. The buoyant jet region is analysed with the assumption of a variable entrainment coefficient in a form corresponding to an approximately constant jet-spreading angle as confirmed by different experimental sources. The properties of surface impingement and internal jump regions are determined on the basis of control volume analyses. Under the Boussinesq approximation, only two dimensionless parameters govern the near-field interaction; these are a discharge densimetric Froude number and a relative depth. For certain parameter combinations, namely those implying low buoyancy and shallow depth, there is no solution to the conjugate downstream condition in the hydraulic jump which would satisfy both momentum and energy conservation principles. Arguments are given which interpret this condition as one which leads to the establishment of a near-field recirculation cell and, thus, discharge instability.

The far-field boundary conditions, while having no influence on discharge stability, determine the bulk mixing characteristics of the jet discharge. The governing equations for the two-layered counterflow system in the far field are solved. The strength of the convective transport, and hence the related dilution ratio, is governed by another non-dimensional parameter, the product of the relative channel length and the boundary friction coefficient.

Experiments in a laboratory flume, covering a range of the governing parameters, are in excellent agreement with the theoretical predictions, both the stability criterion and the bulk mixing characteristics.

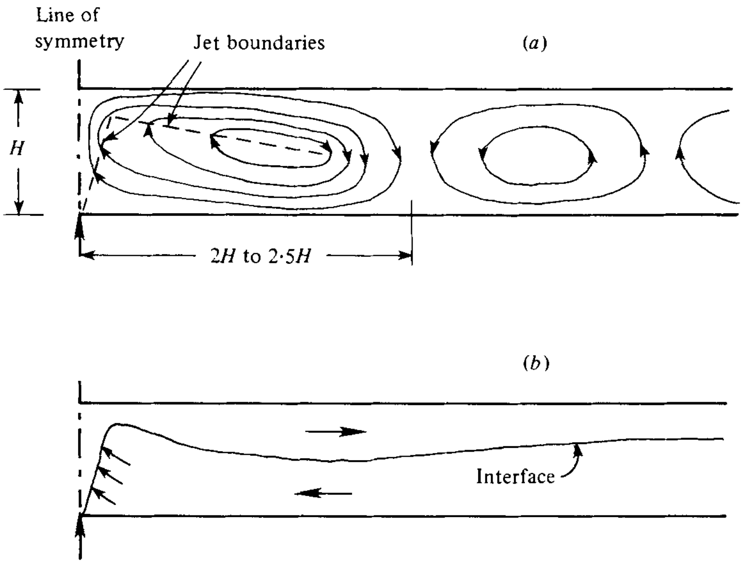

FIGURE 1. Steady-state flow fields for jet discharges into confined depth. (a) Non-buoyant injection. (b) Strongly buoyant injection.

1. Introduction

Depending on the role of buoyancy, the continuous injection of marked fluid in the form of a turbulent jet into an ambient fluid of limited vertical dimension can result in a wide range of flow patterns and associated species distributions. The particular geometry which is considered in this paper is the plane buoyant jet discharging vertically from a slot of constant width into a channel or duct of constant width and limited depth but large horizontal extent. The jet is characterized by a given flux of momentum, volume, buoyancy and mass of a conservative species. The degree of mixing of the species with the ambient fluid is of concern in a number of applications, as will be noted in the following.

Considering first the case of a *non-buoyant discharge*, it is obvious that the concentrated line source of momentum gives rise to internal circulations which extend over the full vertical extent of the channel. These circulations, which are indicated schematically in figure 1(*a*), have been demonstrated in experiments by Iamandi & Rouse (1969), Cola (1966), Murota & Muraoka (1967) and others. The flow structure consists of circulation cells of alternate rotation. The primary cell consists of the upward jet path, the deflected jet along the upper boundary and an entrainment return flow in the remainder of the cell. Experimental observations indicate a primary cell length scale of $2H$ to $2{\cdot}5H$. This length scale and the total mass flow in the primary cell is largely dominated by turbulent jet growth characteristics and the associated entrainment mechanism. This can be shown as follows. Free turbulent jets show a linear growth with distance from the source. Representing the jet as a pure momentum source with zero initial volume flux, this is denoted by $b = ks$, where s is the distance from the source, b is the half mean width of the induced turbulent zone and k is the tangent of the spreading angle in the order of 0·2 (Abramovich 1963). As a first approximation and in analogy to impinging free jets, it may be assumed that the fluid momentum is conserved after impingement and the same geometric behaviour holds for the deflected jet portion as for the initial portion. Thus, the total jet width becomes equal to one half the total depth at a distance from the source $s = 2{\cdot}5H$ or at a longitudinal position $1{\cdot}5H$. The breakdown of the jet behaviour must occur at this point since the velocities in the return flow become equal to the jet velocities. This flow reversal zone has a characteristic radius of $0{\cdot}5H$. Hence, the horizontal length of the primary eddy is estimated as $2H$, which compares well with the observations. The induced volume flux q for a line momentum jet is related to the momentum source m, $q = (2\alpha ms)^{\frac{1}{2}}$, where α = entrainment coefficient (Morton, Taylor & Turner 1956) in the order of 0·07 for the assumption of a normal velocity distribution in the jet. Hence for the total jet length, $s = 2{\cdot}5H$, the circulation in one of the two primary cells is in the order $0{\cdot}6(mH)^{\frac{1}{2}}$, which is in excellent agreement with the available experimental results. Thus, it can be concluded that the primary cell dynamics are self-similar and controlled by the free turbulent characteristics of the jet motion. Effects of wall turbulence due to presence of solid boundaries are negligible for sufficiently high Reynolds numbers (Iamandi & Rouse 1969). Also the effect of a finite slot width B will be small as long as the submergence H/B is large, say > 100. Turbulent momentum transfer at the outer boundary of the primary cell drives the secondary cell as shown by Iamandi & Rouse's experiments. This circulation, however, is about an order of magnitude smaller than in the primary cell. Correspondingly, the kinetic energy content is much less. Even though experimental evidence is lacking so far, it may be expected that higher-order turbulent cells, each with a characteristic length H, will be established. At least qualitatively, this cell structure appears to be similar to the viscous shear transfer in laminar cavity flow, observed by Pan & Acrivos (1967). The dynamics of jet-induced flows are of interest for the design of mixing chambers, reaction tanks, and stilling basins for energy dissipation, amongst others. If a conservative species is injected with the jet, there will be an unsteady build-up of species concentration because of the re-entrainment process in the primary cell.

A radically different flow pattern is generated by a *strongly buoyant discharge* into an unstratified ambient layer of finite depth as indicated in figure 1 (*b*). Basically, the flow consists of a vertically rising buoyant jet followed after impingement by a horizontally spreading surface layer. The buoyant jet (alternatively called a forced plume) is driven by its initial momentum and the buoyant acceleration, and represents the zone of effective entrainment and thus dilution of the injected species concentration. Its behaviour can be taken as independent of the surface layer and can be analysed with the entrainment hypothesis proposed by Morton *et al.* (1956) and further modified by later investigators. The two-dimensional horizontal flow of a buoyant fluid layer has been treated in studies by Ellison & Turner (1959), Wilkinson & Wood (1971), Koh (1971) and Chu & Vanvari (1976). Depending on upstream (that is, in this case after jet impingement) and downstream conditions, the flow can exhibit either a strong depth change – in the form of an internal hydraulic jump or in the form of a horizontal jet zone with buoyant damping of the vertical entrainment flow – or a gradually varying thickness in the form of a stable layer with negligible entrainment. Practical applications of such buoyant injections are plumes from cooling-tower rows in a limited atmosphere with inversions, the spreading of line fires under a ceiling and the discharge into the ocean of sewage (for a review see Koh & Brooks, 1975) or cooling water (for reviews see Harleman & Stolzenbach, 1972, and Jirka, Abraham & Harleman, 1975). In these applications the prediction of species mixing is generally restricted to the analysis of the vertical buoyant jet and it is assumed that no dynamic interaction with the surface layer occurs. This latter assumption is usually made in view of the large horizontal extent of the receiving ambient. The only exception to this state of affairs is the study by Baines & Turner (1969) who treated, amongst others, the case of a plane jet in a two-dimensional vertically and horizontally confined region. This, of course, represents an extreme case of interaction due to the gradual displacement of ambient fluid with the diluted effluent.

This paper is concerned with the analysis of these highly divergent flow patterns and mixing characteristics. The steady discharge of plane turbulent jets with variable buoyancy into a two-dimensional channel of variable depth and length will be considered. The channel opens into a large reservoir, thereby providing a well-defined boundary condition in form of a virtual control for the horizontal buoyant flow and ensuring a steady flow pattern. The particular analytical objective is the development of a criterion for *discharge stability*. A stable discharge configuration will be defined as one in which a buoyant surface layer is formed which does not communicate with the buoyant jet zone. On the other hand, the discharge is unstable whenever a recirculating cell exists in the discharge vicinity. A derived objective is the analysis of the steady-state *mixing characteristics* for an injected conservative substance for both stable and unstable discharge configurations.

2. Qualitative description of the model

Before a detailed theory is developed in § 3 and § 4, it will be useful to give a qualitative description of the model based on the insight into the flow structure gained from laboratory experiments. The quantitative results from these experiments will be used later in § 5 to test the theoretical predictions.

2.1. *Laboratory experiment*

The experiment is performed by injecting heated water at a steady rate through a slot located at the bottom and at the centre of a channel of finite length and perpendicular to the channel axis. The channel is formed simply by inserting a false wall into a laboratory flume: the space between the false wall and the forward wall of the flume then constitutes the 'channel' while the remainder and major portion of the flume forms a large 'reservoir' (figure 2). The channel fluid is initially quiescent with homogenous density ρ_a. The induced flow structure can be visualized by adding neutrally buoyant dye at a constant rate to the jet discharge and taking photographs of the dye pattern through the glass wall of the flume. Figure 3 (plate 1) shows the symmetric flow structure for a stable discharge configuration for a buoyant jet with a densimetric Froude number $F_0 = U_0[(\Delta\rho_0/\rho_a)gB]^{-\frac{1}{2}} = 26{\cdot}3$ and a submergence $H/B = 190$, where U_0 is the injection velocity, $\Delta\rho_0/\rho_a$ the relative density difference between heated water and the ambient, g the gravitational acceleration, B the slot width and H the channel depth. Figure 3 (*a*) demonstrates the impingement process with a thin initial layer being formed at the surface. Some time later, Figure 3 (*b*), the dyed water indicates the formation of a stable stratified layer which flows away in both directions and whose thickness is considerably larger than in the impingement zone. The complete

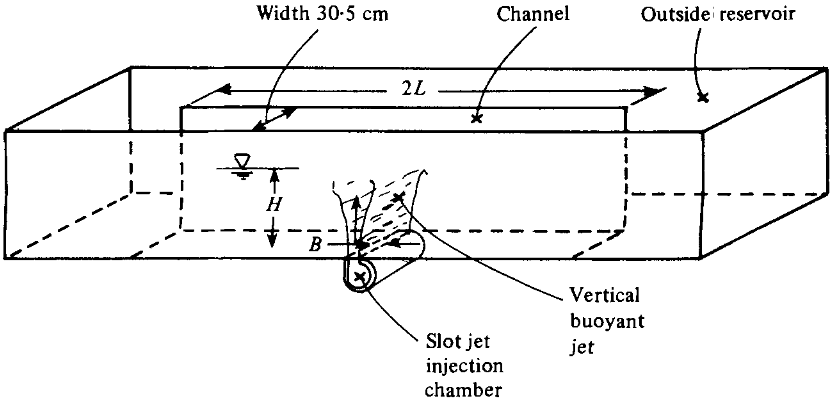

FIGURE 2. Schematics of experimental apparatus.

steady-state flow field is shown in Figure 3 (*c*), including the decreasing thickness of the stratified layer flow at both channel ends which indicates the existence of a virtual control section.

A corresponding sequence is shown in figure 4 (plate 2) for a discharge of higher inertia, less buoyancy and less submergence, $F_0 = 91{\cdot}4$, $H/B = 126$. An unstable discharge configuration can be seen. Following the impingement process, figure 4 (*a*), a circulation cell is formed which extends over the entire channel depth, figure 4 (*b*). The steady-state configuration, figure 4 (*c*), shows the recirculation cells around the vertical discharge, which are occupied by dyed water and have an approximate length $2{\cdot}5H$, and a stable stratified region outside the circulation cells, in which dyed water is flowing toward the reservoir and clear water is flowing underneath from the reservoir toward the recirculation cells. The existence of a virtual control with abrupt layer-thickness change can be clearly seen at the channel ends. All of the unstable experiments, even those with very little buoyancy, exhibited only one recirculation cell. No secondary cells, similar to those occurring in the completely non-buoyant case (see § 1), were observed.

2.2. *Model schematization*

In principle, one might conceive of two approaches toward a stability analysis of buoyant jet discharges into confined depth. First, starting with the condition of zero buoyancy, a model for the multiple circulation structure induced by a turbulent jet is derived. The increasing introduction of discharge buoyancy into such a model will have the effect of progressively suppressing the circulation cells, as the buoyancy force counteracts the inertia of the cell motion. The critical condition of a stable discharge is reached when the innermost primary cell has been suppressed. The second approach proceeds in the reverse manner: a model for the stable discharge configuration which includes the horizontal surface layer spreading after impingement is derived. Then, decreasing the discharge buoyancy, i.e. increasing the discharge densimetric Froude number, will eventually lead to an instability and formation of the primary recirculation cell. This condition is attained when the inertia forces overcome the stabilizing effect of buoyancy. The latter approach has been adopted in this paper.

The flow structure for a stable discharge configuration can for analytical purposes be schematized into four regions, as shown in figure 5: I, buoyant jet region; II, surface

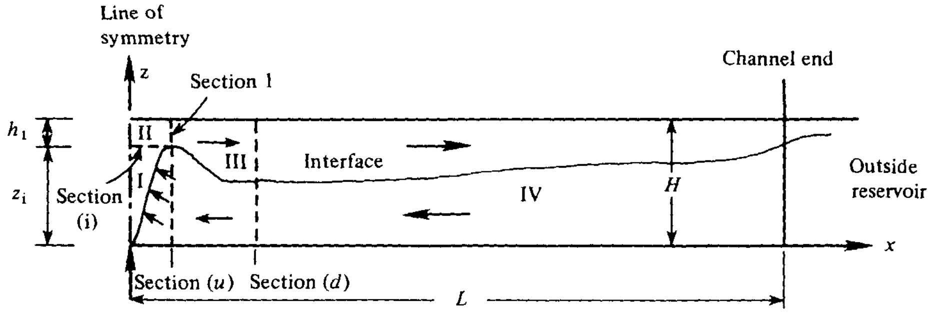

FIGURE 5. Schematization of flow field under stable discharge configuration: I, buoyant jet region; II, surface impingement region; III, internal hydraulic jump region; IV, stratified counterflow region.

impingement region; III, internal hydraulic jump region; and IV, stratified counterflow region. This idealization is suggested by the qualitative experimental evidence (see figure 3*c*). These regions are analysed sequentially using simplified versions of the general governing equations. The inter-region boundaries are unknown *a priori* and are determined analytically.

The Boussinesq assumption will be adopted in all regions. This means that attention is restricted to cases in which the induced density deviations are small compared to the total fluid density, an assumption which holds for most environmental applications (Turner 1973). Thus, any densimetric Froude number $F = U[(\Delta\rho/\rho_a)gH]^{-\frac{1}{2}}$ is finite while a free-surface Froude number $F^* = U(gH)^{-\frac{1}{2}} \ll 1$ is negligible, where U, H, $\Delta\rho/\rho$ are characteristic velocity, length and density deficiency scales, respectively. As a consequence, the deformation of the free surface above the impinging jet can be neglected. Thus, the schematization given in figure 5 is equally applicable for a duct or cavity with a flat top or, if the z axis is turned around, for a dense jet discharging vertically downward. Any differences due to the additional boundary shear in these cases can be accounted for in the theory.

3. Stability analysis

3.1. *Governing equations*

The flow is incompressible and turbulent but steady in the mean. The time-averaged velocity field is two-dimensional with velocities u and w in the horizontal direction x and in the vertical direction z, respectively. The time-averaged induced temperature is $T(x,z)$ while the homogeneous ambient temperature is T_a. The excess temperature, i.e. the difference $\theta(x,z) = T(x,z) - T_a$, will be treated as a conservative tracer concentration. This is equivalent to the neglect of external heat losses. An equation of state links the induced density changes $\rho(x,z) - \rho_a$ to the tracer concentration

$$(\rho_a - \rho(x,z))/\rho_a = \beta\theta(x,z), \tag{1}$$

where β is the coefficient of expansion. β may be a function of $\theta(x,z)$, but is assumed constant in good approximation for cases with limited temperature ranges. Molecular transport of momentum and tracer is neglected in comparison to the turbulent transport.

With these assumptions, the governing equations are the equations of continuity

$$\partial u/\partial x + \partial w/\partial z = 0, \tag{2}$$

momentum conservation

$$u\frac{\partial u}{\partial x} + w\frac{\partial u}{\partial z} = -\frac{1}{\rho_a}\frac{\partial p}{\partial z} - \frac{\partial \overline{u'^2}}{\partial x} - \frac{\partial \overline{u'w'}}{\partial z} \tag{3}$$

and

$$u\frac{\partial w}{\partial x} + w\frac{\partial w}{\partial z} = -\frac{1}{\rho_a}\frac{\partial p}{\partial z} - \frac{\rho - \rho_a}{\rho_a}g - \frac{\partial \overline{u'w'}}{\partial x} - \frac{\partial \overline{w'^2}}{\partial z}, \tag{4}$$

and tracer conservation

$$u\frac{\partial \theta}{\partial x} + w\frac{\partial \theta}{\partial z} = -\frac{\partial \overline{u'\theta'}}{\partial x} - \frac{\partial \overline{w'\theta'}}{\partial z}. \tag{5}$$

In these equations, p denotes the mean dynamic pressure deviation from hydrostatic conditions and the primed quantities represent the turbulent fluctuations from the mean flow variables.

3.2. *Buoyant jet region*

The vertical injection of fluid with velocity U_0 and buoyant acceleration $\beta\theta_0 g$ generates within a narrow zone a fluid motion which is associated with strong shear effects and intense turbulence and which grows as non-turbulent outside fluid is entrained into this zone. The induced approach velocities in the outer region are considerably weaker than the mean jet velocities and their distribution depends on the ambient geometry. At its upper end, the buoyant jet region is bounded by the surface impingement region in which the vertical current ultimately stagnates, giving rise to significant pressure disturbances. The jet region itself will be assumed to be free of these pressure effects (see later in §3.3) and the governing equations can be simplified considerably if the usual boundary-layer approximations (Schlichting 1968) are introduced: (1) vertical velocities dominate over lateral ones, $w/u \gg 1$; (2) dynamic pressure effects within the turbulent zone are negligible, $p \approx 0$; (3) the vertical turbulent diffusion of momentum and mass is negligible compared to the convective transport by the mean motion. The later approximation in application to buoyant jets has been questioned by Priestley & Ball (1955) and, in particular, by Kotsovinos & List (1977) who measured the buoyant jet flux properties and found an appreciable fraction transported in the form of turbulent diffusion. However, in the later stage of the analysis, experimentally determined coefficients are introduced which apparently compensate for this deviation.

The simplified equations of motion can be further reduced to ordinary differential equations as a function of vertical distance z by integrating laterally across the buoyant jet. This basic procedure has been followed in several studies on buoyant jets and their limiting stages, the pure plume and the pure momentum jet, beginning with the early work of Priestley & Ball (1955), Morton *et al.* (1956) and Schmidt (1957). Since the prediction of the transition properties of the buoyant jet has an ultimate bearing upon the problem of discharge stability in a confined depth, the different approaches toward the integral analysis are critically examined herein, in particular from the viewpoint of experimental evidence. For purposes of the lateral integration, the distribution of vertical velocity and tracer in the jet zone is expressed as

$$w(x,z) = w_c(z)f(\eta), \quad \theta(x,z) = \theta_c(z)g(\eta) \tag{6}$$

where w_c and θ_c are values of w and θ at the centre, respectively. η is the normalized lateral distance $\eta = x/b$ where b is a measure of the local lateral spread of the jet; f and g are suitable functions which approximate the observed bell-shaped profiles within the zone. This allows the definition of three integral flux properties,

$$\begin{aligned} q(z) &= I_1 w_c b \quad \text{volume flux}, \\ m(z) &= I_2 w_c^2 b \quad \text{momentum flux}, \\ q_\theta(z) &= I_3 w_c \beta g \theta_c b \quad \text{buoyancy flux}, \end{aligned} \tag{7}$$

where I_1, I_2 and I_3 are profile-dependent coefficients,

$$I_1 = \int_{-\infty}^{\infty} f\, d\eta, \quad I_2 = \int_{-\infty}^{\infty} f^2\, d\eta \quad \text{and} \quad I_3 = \int_{-\infty}^{\infty} fg\, d\eta.$$

The integrated equations of motion are

$$\frac{dq}{dz} = 2(-v_e), \quad \frac{dm}{dz} = I_4 \beta g \theta_c b \quad \text{and} \quad \frac{dq_\theta}{dz} = 0, \tag{8}$$

where v_e is the lateral approach velocity at the jet periphery representing the entrainment and

$$I_4 = \int_{-\infty}^{\infty} g\, d\eta$$

is another profile-dependent coefficient. In a free turbulent shear region the turbulent velocities, and hence the entrainment velocity, can be expected to be proportional to the characteristic velocity difference across the shear region. This argument was first applied to the analysis of the buoyant plume by Morton *et al.* (1956) who proposed $(-v_e) = \alpha w_c$, where α is the entrainment coefficient. With this proposition, the equation set (8) becomes in terms of the integral variables q, m amd q_θ

$$\frac{dq}{dz} = 2\alpha \frac{I_1}{I_2} \frac{m}{q}, \quad \frac{dm}{dz} = \frac{I_2 I_4}{I_1 I_3} \frac{q q_\theta}{m} \quad \text{and} \quad \frac{dq_\theta}{dz} = 0. \tag{9}$$

Only for self-similar flow can the coefficients in the above set be considered constant. Indeed, only the limiting forms of the buoyant jet are self-similar motions: in the pure jet (Tollmien 1926), there exists a constant internal balance between momentum and turbulent friction and, in the pure plume (Schmidt 1941), between momentum, buoyancy and turbulent friction. The buoyant jet which is in transition between these limiting cases therefore has a variable internal force balance and thus the jet coefficients should in principle be a function of position z. The variability of the coefficients and its impact on practical applications must be assessed on the basis of experimental information. Before considering this, an alternative linearly dependent equation set is considered by using the width $b = I_2 I_1^{-2} q^2 m^{-1}$ in the place of the volume flux q. Upon differentiation with respect to z, the following growth equation is obtained:

$$\frac{db}{dz} = \frac{4\alpha}{I_1}\left(1 - \frac{I_1 I_4}{4\alpha I_2} \frac{1}{F_l^2}\right), \tag{10}$$

where F_l is a densimetric Froude number as a measure of the local force balance within the buoyant jet

$$F_l^2 = \frac{w_c^2}{\beta g \theta_c b} = \frac{I_3}{I_2^{\frac{3}{2}}} \frac{m^{\frac{3}{2}}}{q_\theta b^{\frac{3}{2}}}. \tag{11}$$

If the right-hand side of (10) is denoted by a spreading coefficient k, which *a priori* is a function of position, then the alternative equation set for b, m and q_θ is

$$\frac{db}{dz} = k, \quad \frac{dm}{dz} = \frac{I_2^{\frac{1}{2}} I_4}{I_3} \frac{q_\theta b^{\frac{1}{2}}}{m^{\frac{1}{2}}} \quad \text{and} \quad \frac{dq_\theta}{dz} = 0. \tag{12}$$

Thus the equation for geometric growth in (12) replaces the equation for growth of the volume flux in (9). The question of the variability between the limiting stages of the coefficients in each equation system is now examined in light of experimental data. First of all, it appears that the normalized profile shapes for pure jets and pure plumes are the same within experimental accuracy. The observed distributions are well approximated with the normal functions

$$f = \exp(-y^2/b^2), \quad g = \exp(-y^2/\lambda^2 b^2), \tag{13}$$

so that b represents the width where the velocity is $1/e$ of the value at the centre. $\lambda > 1$ is a turbulent dispersion ratio between tracer and velocity and is equal to the inverse of the square root of the turbulent Prandtl number. The shape coefficients are then independent of position z:

$$I_1 = \pi^{\frac{1}{2}}, \quad I_2 = (\pi/2)^{\frac{1}{2}}, \quad I_3 = \lambda[\pi/(1+\lambda^2)]^{\frac{1}{2}}, \quad I_4 = \lambda\pi^{\frac{1}{2}}. \tag{14}$$

Thus the only coefficients which remain as functions of the internal force characteristics of the buoyant jet, i.e. its local Froude number F_l, are α and λ in (9) or k and λ in (12).

Available data for the *pure jet*, $F_l = \infty$, have been discussed by Abraham (1963) and, more recently, Kotsovinos (1976). Observed values for the jet spreading rate k_j show some increase with distance z/B as commented upon by Kotsovinos (1976) and Bradshaw (1977). The value of $k_j = 0{\cdot}154$, based upon Albertson *et al.* (1950), is adopted here as representative over a large region z/B. The corresponding entrainment coefficient is $\alpha_j = I_1 k_j/4 = 0{\cdot}069$ by virtue of (10) and (12*a*). Measurements by van der Hegge Zijnen (1958) suggest a value $\lambda_j = 1{\cdot}46$ in close agreement with the value $\surd 2$ from Taylor's mixing-length theory.

The self-similar motion in a *pure plume* is characterized by a constant Froude number $F_l = F_{lp}$. The value of F_{lp} can be found by taking the derivative of (11) with respect to z and making use of (12):

$$\frac{dF_l^2}{dz} = \frac{3}{2}\frac{k}{b}\left[\frac{I_4}{kI_2} - F_l^2\right]. \tag{15}$$

Thus, in the asymptotic plume stage,

$$F_{lp} = \left(\frac{I_4}{k_p I_2}\right)^{\frac{1}{2}}, \tag{16}$$

where the k_p is the spreading rate for the pure plume. Rouse, Yih & Humphreys (1952) derived $k_p = 0{\cdot}177$ and $\lambda_p = 0{\cdot}89$ based on their analysis of plume data, leading by virtue of (10), (12*a*) and (16) to the frequently quoted value $\alpha_p = \frac{1}{2}I_2 k_p = 0{\cdot}16$ (Morton 1969). However, Abraham (1963) pointed out deficiencies in Rouse *et al.*'s original analysis. His re-analysis suggested the alternative, and physically more appealing ($\lambda > 1$), values $k_p = 0{\cdot}147$ and $\lambda_p = 1{\cdot}24$. From this it can be deduced that

$$\alpha_p = 0{\cdot}130 \quad \text{and} \quad F_{lp} = 3{\cdot}45.$$

Therefore, mere consideration of the limiting stages of the buoyant jet shows the following variability: $k_p/k_j = 0{\cdot}95$, $\lambda_p/\lambda_j = 0{\cdot}85$, and $\alpha_p/\alpha_j = 1{\cdot}88$. Thus, in first approximation, it seems reasonable to take $k = k_p$ and $\lambda = \lambda_p$, so that all coefficients in (12) are constant. Recent measurements by Kotsovinos & List (1977) on the complete transition in a buoyant jet strongly support the approximation of constant spreading and of a constant dispersion ratio along the jet path. They found $\lambda = 1{\cdot}35$ and $k = 0{\cdot}116$, which is somewhat smaller than the earlier values for the limiting stages and may reflect the effect of initial flow adjustment problems owing to a low z/B range and of a small jet efflux Reynolds number (see also Kotsovinos 1976). The solution of (12) for the boundary values b_0, m_0, $q_{\theta 0}$ and F_{l0} at $z = 0$ is, with $z' = zk/b_0$,

$$\left.\begin{aligned} b &= b_0(z'+1), \\ m &= m_0\left\{1+\frac{F_{lp}^2}{F_{l0}^2}\left[(z'+1)^{\frac{3}{2}}-1\right]\right\}^{\frac{2}{3}} \\ \text{and}\qquad q_\theta &= q_{\theta 0}. \end{aligned}\right\} \tag{17}$$

By virtue of the relation $q = I_1 I_2^{-\frac{1}{2}}(mb)^{\frac{1}{2}}$ the volume flux ratio is calculated from the above as

$$q = (2\pi)^{\frac{1}{4}}(m_0 b_0)^{\frac{1}{2}}\left\{1+\frac{F_{lp}^2}{F_{l0}^2}\left[(z'+1)^{\frac{3}{2}}-1\right\}^{\frac{1}{3}}(z'+1)^{\frac{1}{2}}. \tag{18}$$

The solutions for the limiting cases are: for the pure jet ($F_{l0} = \infty$)

$$m = m_0, \quad q = (2\pi)^{\frac{1}{4}}(m_0 b_0)^{\frac{1}{2}}(z'+1)^{\frac{1}{2}}; \tag{19}$$

and for the pure plume ($F_{l0} = F_{lp}$)

$$m = m_0(z'+1), \quad q_\theta = q_{\theta 0}, \quad q = (2\pi)^{\frac{1}{4}}(m_0 b_0)^{\frac{1}{2}}(z'+1). \tag{20}$$

A special case of (17) and (18) is the buoyant jet from a line source, m_0, $q_{\theta 0}$, $q_0 = 0$, $b_0 = 0$ at $z = 0$,

$$b = kz, \quad m = m_0\left\{1+\frac{I_2^{\frac{1}{2}} I_4}{I_3}\frac{q_{\theta 0} k^{\frac{1}{2}}}{m_0^{\frac{3}{2}}} z^{\frac{3}{2}}\right\}^{\frac{2}{3}},$$

and

$$q_\theta = q_{\theta 0}, \quad q = \frac{I_1}{I_2^{\frac{1}{2}}} m_0^{\frac{1}{2}} k^{\frac{1}{2}}\left\{1+\frac{I_2^{\frac{1}{2}} I_4}{I_3}\frac{q_{\theta 0} k^{\frac{1}{2}}}{m_0^{\frac{3}{2}}} z^{\frac{3}{2}}\right\}^{\frac{1}{3}} z^{\frac{1}{2}}. \tag{21}$$

The solutions (17) and (18) are similar to those of Schmidt (1957) and Abraham (1965), except for minor differences in the initial conditions to account for the jet flow establishment. Comparison of (17) and (18) with experimental data on buoyant jets shows excellent functional agreement (Kotsovinos & List 1977).

The alternative assumption of a constant entrainment coefficient α and use of (9) seems less satisfactory in view of the experimental data. In fact, it implies a spreading rate for the pure jet which is twice as large as for the pure plume as shown by Lee & Emmons (1961). This can be seen directly from (10). List & Imberger (1973, 1975; see also Abraham & Jirka, 1974) have proposed a variable entrainment function to reconcile the apparent variability of α. Different functional forms, which provide a transition in α between the pure jet and the pure plume values depending upon F_l, can be applied. One of these functions, which can be directly deduced from (10) and (12*a*) with constant k, has been used by Kotsovinos & List (1977) to solve (9). The solutions are identical to (17) and (18) as expected.

In order to compare with the experimental results in § 5, the actual source conditions with total slot width B, uniform velocity U_0 and uniform tracer concentration θ_0, must be related to the assumed conditions of a fully developed jet profile at $z = 0$. With $m_0 = U_0^2 B$ and $q_{\theta 0} = \beta g \theta_0 U_0 B$ it is found that $b_0 = B/I_2$ and $F_{l0}^2 = I_3 F_0^2$, where $F_0 = U_0(\beta g \theta_0 B)^{-\frac{1}{2}}$ is the actual source densimetric Froude number. This assumes an initial volume flux $q_0 = I_1 I_2^{-1}(U_0 B)$ which is larger than the actual volume flux $U_0 B$, since $I_1 I_2^{-1} = \sqrt{2}$. In reality, this increased flux is approached at the end of the zone of flow establishment in which an adjustment takes place from the initial uniform efflux profiles to the jet profiles. Neglect of this zone which has an approximate length $5B$ (Albertson *et al.* 1950) seems justifiable only if the total jet submergence H/B is large.

3.3. *Surface impingement region*

In this region a complicated transition takes place from the vertical jet flow to a horizontal spreading motion. A control volume analysis is carried out to describe the bulk features of the transition, in particular the thickness h_1 of the spreading layer. The control volume (figure 5) is chosen so as to satisfy the following approximations: (1) The inflow at the lower boundary [section (i)] of the control volume, $z_i = H - h_1$, has the characteristics for the buoyant jet region, i.e. fully established profiles and zero dynamic pressure. (2) No additional entrainment occurs, i.e. the sides of the control volume (section 1) are taken close to the boundaries of the vertical jet. (3) The density and velocity distributions at section 1 are taken as uniform over the depth of the spreading layer. This assumption is borne out by experimental observations (§ 5) for the case of discharges with buoyancy. The purely non-buoyant case has more jet-like velocity distributions within the spreading layer (Cola 1966; Murota & Muroako 1967) but is of no interest for purposes of the stability analysis.

The governing equations for the control volume are an energy equation (datum at $z = 0$)

$$\frac{\overline{u_i^2}}{2} - \beta g \overline{\theta}_i z_i = \frac{u_1^2}{2} - \beta g \theta_1 \left(H - \frac{h_1}{2} \right) + g h_L; \tag{22}$$

a continuity equation

$$q_i = 2 u_1 h_1; \tag{23}$$

and a tracer conservation equation

$$q_{\theta i} = 2 \beta g \theta_1 u_1 h_1. \tag{24}$$

The two profile-averaged terms at the inflow section in (22) are expressed as

$$\overline{u_i^2} = I_5 w_{c_i}^3 b_i / q_i,$$

where w_{c_i} is the centre-line velocity and b_i the jet width at section (i) and $I_5 = \int_{-\infty}^{\infty} f^3 \, d\eta$ which takes on the value $I_5 = (\frac{1}{3}\pi)^{\frac{1}{2}}$ for the normal profile, and as $\beta g \overline{\theta}_i = q_{\theta i}/q_i$, respectively. (22) also contains a term $g h_L$ which describes the loss of energy due to secondary turbulent motions in the transition. This energy loss can be related to the

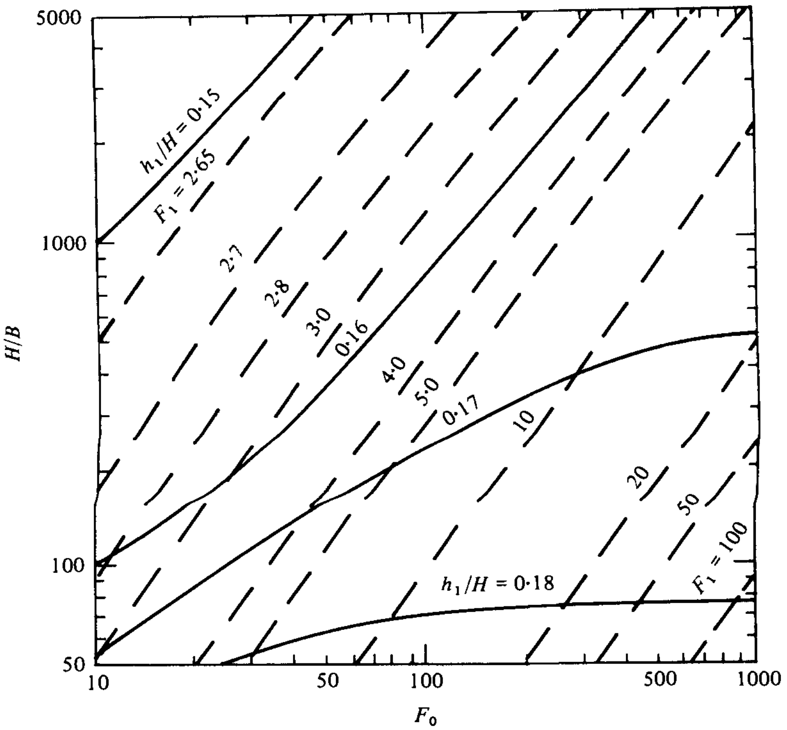

FIGURE 6. Thickness h_1/H and spreading Froude number F_1 of surface impingement layer as a function of discharge conditions F_0 and H/B.

inflow energy as $gh_L = \frac{1}{2}K_L\overline{u_1^2}$ and estimates of the loss coefficient K_L can be obtained by considering the qualitatively similar transition in flow in closed conduit bends. For example, the measurements by Ito (1960) suggest a value $K_L \sim 0{\cdot}2$ for a wide range of curvatures in 90° transitions.

The spreading-layer depth h_1 is obtained from (22), (23) and (24) in terms of the jet integral values b_i, m_i, q_i and $q_{\theta i}$:

$$(1-K_L)\frac{I_5}{I_1 I_2}\frac{m_i q_i}{b_i q_{\theta i} h_i} = \frac{q_i^3}{4h_1^3 q_{\theta i}}. \tag{25}$$

Upon substitution of the jet solutions (17) and (18), the relative layer depth h_1/H can be solved for numerically. Figure 6 gives h_1/H as a function of the discharge parameters F_0 and H/B for a value $K_L = 0{\cdot}2$. Another dynamic parameter, the Froude number of the spreading layer, $F_1^2 = u_1^2(\beta g\,\theta_1 h_1)^{-1}$ or alternatively $F_1^2 = q_i^3(4q_{\theta i}h_1^3)^{-1}$, is also included in figure 6.

The two limiting discharge cases are considered to demonstrate the solution sensitivity to the energy loss coefficient K_L and to the effect of buoyancy. For the *pure jet*, $F_0 = \infty$ and for line source conditions (21), an explicit solution of (23) is

$$h_1/H = \left\{1 + \frac{2}{k}\left[\frac{(1-K_L)\,I_5}{I_1^3}\right]^{\frac{1}{2}}\right\}^{-1}, \tag{26}$$

where k is the spreading coefficient. With the usual integral constants the following limited sensitivity is found, for $K_L = 0$, $0{\cdot}2$ and $0{\cdot}4$, $h_1/H = 0{\cdot}146$, $0{\cdot}161$ and $0{\cdot}181$ respectively. The value $K_L = 0{\cdot}2$ is adopted in the further analysis. For the *pure plume*, $F_0 = 2{\cdot}94$, and, for line conditions, (25) becomes

$$(1-K_L)\,I_5 = \frac{F_1^3\,k^2}{4}\left(\frac{H}{h_1}-1\right)^2 - \frac{I_2\,I_3}{I_4}\left(\frac{H}{h_1}-1\right)^{-1}, \tag{27}$$

which yields $h_1/H = 0{\cdot}150$ for $K_L = 0{\cdot}2$. Thus, the effect of buoyancy on the spreading conditions is relatively small (of the order of 10 %). The associated spreading Froude number F_1 is $F_1 = 2{\cdot}64$.

Figure 6 includes the limiting conditions for the pure plume in the range of low F_0 and high H/B. The predictions for h_1/H in the weakly buoyant range of high F_0 and low H/B deviate slightly from the line solution (26) due to the effect of the finite source conditions. Figure 6 describes the flow conditions prior to the hydraulic jump.

3.4. *Internal hydraulic jump region*

The vertical section following the impingement zone [section (u) in figure 5] exhibits a high velocity spreading flow in the thin upper layer, h_1, and a low velocity return flow in the lower layer, $h_2 = H - h_1$. Further attention is limited to high degrees of buoyant jet mixing, $q_i/q_0 \gg 1$, so that equal counterflow, $q_1 = -q_2$, can be assumed. Forming the sum of the squares of the Froude numbers of the two-layer stratified flow

$$S_u = F_1^2 + F_2^2, \tag{28}$$

where $F_2^2 = q_2^2(\beta g\,\theta_1\,h_2^3)^{-1}$, it can be seen from figure 6 that

$$S_u > 1. \tag{29}$$

Thus, section (u) represents a supercritical condition in stratified flow (Schijf & Schonfeld 1953; Harleman 1960; Yih 1965; Long 1972) and S_u will be called the supercriticality of the system. Supercritical flow, in analogy to compressible flow, can undergo rapid transitions in its flow conditions in form of a shock wave, or hydraulic jump, which preserves fluid momentum while dissipating mechanical energy. The occurrence, and the position, of hydraulic jumps is governed by the existence of a downstream blocking effect or control. The stratified subcritical counterflow (region IV) with a control section at the channel end represents such a blocking effect and fixes the jump position close to the impingement region.

Before proceeding with the jump analysis it is essential to consider another possibility of a supercritical flow transition in a miscible fluid system, that is, by virtue of turbulent vertical entrainment. This possibility was discussed in detail by Wilkinson & Wood (1971) for the simpler case of only one layer flowing supercritically. Generally, Wilkinson & Wood found an entrainment zone followed by the actual jump zone ('roller region'). The length of the entrainment zone is determined by the downstream control. A strong downstream control eliminates the entrainment zone and a pure hydraulic jump with negligible entrainment occurs. A similar flow field has been observed in the present investigation under stable discharge conditions, i.e. sufficiently high buoyancy. If the discharge conditions are less buoyant, and therefore unstable, there is indeed significant jet-like entrainment in the spreading flow as discussed in the introductory paragraphs.

The hydraulic jump analysis describes the flow change between two conjugate sections, the upstream section (u) and the downstream section (d). Following Yih & Guha (1955) the momentum conservation equations are written for the two layers, neglecting shear forces at the surface, interface or bottom and assuming hydrostatic conditions, uniform velocity distributions and zero entrainment,

$$\left.\begin{aligned} 2q_1^2(h_1-h_1') &= h_1 h_1'(h_1+h_1')\,g[(h_1-h_1')+(h_2-h_2')] \\ \text{and}\qquad 2q_2^2(h_2-h_2') &= h_2 h_2'(h_2+h_2')\,g[(1-\beta\theta_1)\,(h_1-h_1')+(h_2-h_2')],\end{aligned}\right\} \tag{30}$$

where h_1' and h_2' are the layer depths at section d, respectively. (30) are valid for a finite density difference, $\beta\theta_1$. The Boussinesq approximation is introduced by equating the expression $[(h_1-h_1')+(h_2-h_2')]/(\beta\theta_1)$ obtained from both equations (30) and letting $\beta\theta_1 \to 0$ in the resulting equation. This yields a constant surface elevation

$$H = h_1+h_2 = h_1'+h_2' \tag{31}$$

and the equation for the upper layer change

$$f(h_1') = \left[\left(\frac{h_1'-h_1}{H-h_1}-\frac{3}{2}\right)^2-\frac{1}{4}\right]\left[1-\frac{2F_1^2h_1^2}{h_1'(h_1'+h_1)}\right]-2F_1^2\left(\frac{h_1'}{H-h_1}\right)^3 = 0, \tag{32}$$

in which the restriction to equal counterflow

$$F_2^2 = F_1^2\left(\frac{h_1}{H-h_1}\right)^3$$

has been made.

Some solution properties of the quartic equation of the above type have been discussed by Long (1970), Mehrotra (1973) and Mehrotra & Kelly (1973). In general, for a given F_1 and (h_1/H) (32) has two solutions within the physical domain $0 < (h_1'/H) < 1$, as is indicated qualitatively by point I and II in figure 7. On the basis of specific energy considerations only solution I, that is, the lower h_1'/H value, is admissible. Defining the downstream property

$$S_d = F_1'^2+F_2'^2, \tag{33}$$

where F_1' and F_2' are the respective Froude numbers after the jump, it can be shown that the admissible solution I satisfies

$$S_d < S_u, \tag{34}$$

which means a decrease in specific energy due to dissipation; solution II satisfies

$$S_d > S_u, \tag{35}$$

which is physically impossible as it would require an external energy input. Increasing the upstream supercriticality S_u, by increasing either F_1 or h_1/H, causes a more pronounced jump and a moving together of the two solutions (dashed line in figure 7). There is a limiting value of S_u for which both solutions merge into one (dot-dashed line in figure 7) satisfying

$$S_d = S_u, \tag{36}$$

i.e. no change in specific energy; and therefore

$$h_1'/H = 1-h_1/H, \tag{37}$$

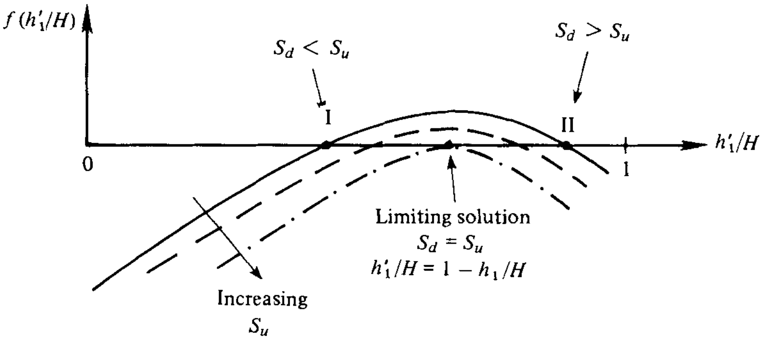

FIGURE 7. Solution properties of internal hydraulic jump equation (32) as a function of upstream supercriticality S_u. Solution I is the general admissible solution with lower specific energy.

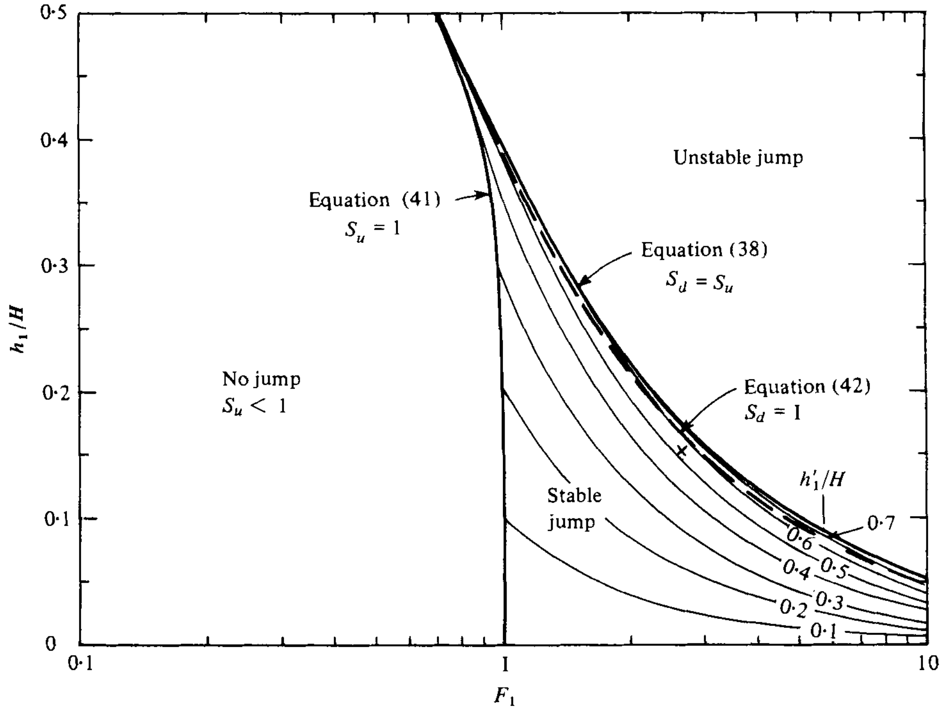

FIGURE 8. Stability plot for internal hydraulic jumps with equal flow in both layers as a function of upstream conditions F_1 and h_1/H (× indicates conditions for pure plume discharge).

i.e. the jump takes on a symmetric shape. Substituting (37) into (32) gives the equation for the limit line

$$\left[\left(\frac{H-2h_1}{H-h_1}-\frac{3}{2}\right)^2-\frac{1}{4}\right]\left[1-\frac{2F_1^2h_1^2}{H(H-h_1)}\right]-2F_1^2\left(\frac{h_1}{H-h_1}\right)^3=0. \tag{38}$$

The complete solution of (32) within the parameter space F_1 and $0 < h_1/H < 0{\cdot}5$ is given in figure 8. No jump can occur if the upstream conditions are subcritical. The critical limit is given by

$$S_u = 1, \tag{39}$$

which implies from (28) and for equal counterflow

$$F_1^2 + F_1^2\left(\frac{h_1}{H-h_1}\right)^3 = 1 \tag{40}$$

so that

$$h_1/H = \left[1 + \left(\frac{F_1^2}{1-F_1^2}\right)^{\frac{1}{3}}\right]^{-1}. \tag{41}$$

The solution for the critical condition, $h_1' = h_1$, can be obtained from (32).

Thus, as can be seen from figure 8, a hydraulic jump is only possible in that F_1 and h_1/H parameter range lying between the solid lines defined by (38) and (41). This region is further subdivided by the dashed line into a zone of subcritical downstream conditions $0 < S_d < 1$ and a zone of supercritical downstream conditions $1 < S_d < S_u$. The equation of the dividing line is from (32) with $S_d = 1$:

$$F_1^{-2}(h_1/H)^{-3} = (h_1'/H)^{-3} + (1-h_1'/H)^{-3}. \tag{42}$$

No solutions which would satisfy the momentum conservation equation are possible for the region of high upstream supercriticality S_u, i.e. in the upper right corner of figure 8. This non-existence of a solution has been discussed by Mehrotra (1973). Mehrotra argues that under this condition 'shocks cannot form and the disturbance (i.e. the flow control) is negotiated purely locally in the manner of an absolutely supercritical flow'. Mehrotra's argument is not convincing for the following reason. If the region of no solution is approached by increasing F_1 while keeping h_1/H constant, it can be seen that the jump intensity, given by the ratio h_1'/h_1, increases (see figure 8). At the edge of the region the jump has a maximum intensity. Thus, on a purely theoretical basis it seems unlikely that the region of no solution would have no tendency to form shocks. On the contrary, it is likely that there is a tendency for an extreme shock formation which, however, cannot be sustained at the downstream section by virtue of the requirement of flow momentum conservation. Physically, this may be interpreted as a condition of downstream flow instability leading to mixing and flow recirculation over the shock region and ultimately to a breakdown of the stratified flow. This interpretation is, in fact, borne out by the experiments. Thus, the region of no solution in figure 8 has been labelled as the 'unstable jump' region in contrast to the regular 'stable jump' region.

The above one-dimensional analysis does not predict the length of the hydraulic jump. Using as a first approximation the analysis of the free surface jump by Mehrotra (1976), the jump length is estimated as $(x_d - x_u) \approx 2H$. Taking for the position of the upstream section $x_u \approx 0{\cdot}5H$ (based on the total jet width at impingement), the downstream section is located at $x_d \approx 2{\cdot}5H$. This estimate will be used in §4 for matching with the counterflow region.

3.5. *Discharge stability*

The hydraulic jump predictions of figure 8 can now be applied to the present problem with the given conditions at the end of the surface impingement region (figure 6). The resultant discharge stability diagram in the F_0 and H/B parameter space is given in figure 9, indicating a region of stable and a region of unstable discharge configurations. The lines of equal conjugate height h_1'/H are also shown for the stable discharge domain. All equal height lines and the limit line are approximately linear, with minor deviations due to initial geometry effects. If the geometry effects are neglected altogether and the

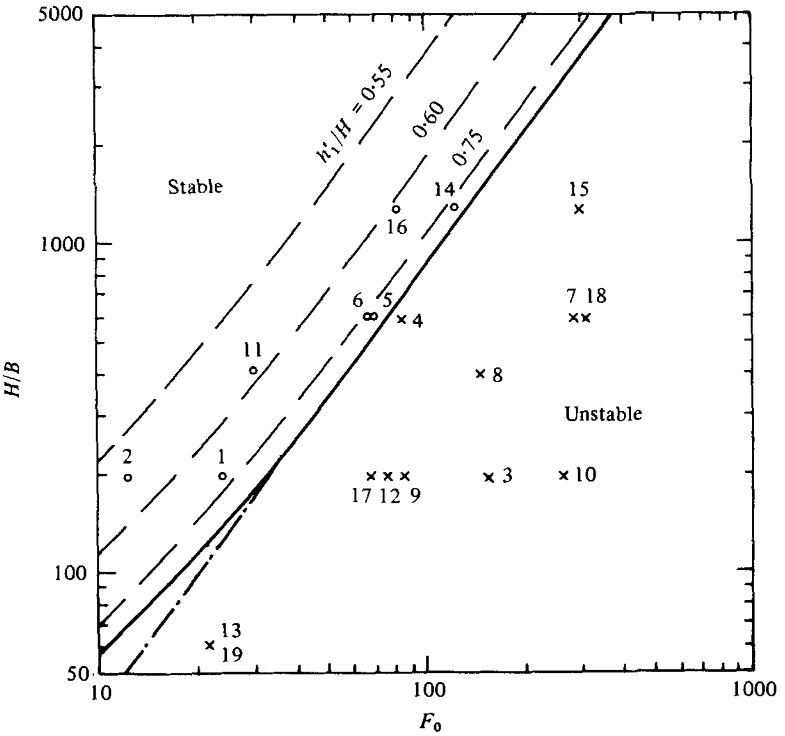

FIGURE 9. Stability diagram for plane buoyant jets discharging into confined depth as a function of F and H/B. ——, stability criterion, —·—·—, equation (44); – – –, conjugate depth in the stable domain. The experimental observations are indicated with ○ for stable and × for unstable; the numbers adjacent to the symbols are the experiment numbers (see table 1).

line source buoyant jet solution (21) is used in the impingement analysis (25), then the limit line can be predicted as

$$\frac{m_0}{q_{\theta 0}^{\frac{2}{3}} H} = 0{\cdot}39 \tag{43}$$

or, in terms of the parameters F_0 and H/B, as

$$F_0 = 0{\cdot}63 \left(\frac{H}{B}\right)^{\frac{3}{4}}. \tag{44}$$

This is in close agreement with the limit curve given in figure 9 except for low H/B, where geometry effects are important.

Of particular interest is the pure plume discharge (low F_0 – high H/B) which falls in the stable discharge domain (see also point × in figure 8) as has been assumed, so far without proof, by previous investigators. The pure plume has a conjugate height of $h_1' = 0{\cdot}52$ or approximately one half of the total depth.

In summary, the discharge stability of a vertical buoyant jet in a shallow layer is determined solely by the dynamics of the three near-field regions and is independent of the boundary conditions in the far-field. The far-field, however, has an influence on the mixing characteristics of the discharge as is shown in the following section.

4. Mixing analysis

4.1. *Near-field and far-field interactions*

The far-field of the problem is given by the gradually varying stratified counterflow influenced by interfacial and boundary friction, with a critical flow section at the channel end (see figure 5). This boundary condition allows for a steady-state behaviour of the discharge as ambient fluid flows in the lower layer toward the discharge region while the mixed buoyant fluid flows into the outside reservoir. Depending on their respective properties, four types of near-field and far-field interactions can be postulated:

(*a*) *Stable discharge.* For a given discharge in each layer q_1 and density difference $\beta\theta_1$ the critical section provides a unique shape for the interfacial depth in the counterflow zone. Of primary importance is the interfacial depth $\hat{h}_1$ at the boundary to the near-field zone $x_d \approx 2{\cdot}5H$ and its relationship to the conjugate jump depth h_1'.

(i) $S_d < 1$, $h_1' \geqslant \hat{h}_1$: This is the normal hydraulic jump behaviour with subcritical downstream conditions. Actually, the conjugate height h_1' is not reached, as the upper layer jumps to the height $\hat{h}_1$.

(ii) $S_d > 1$, $h_1' \geqslant \hat{h}_1$: Theoretically, a jump occurs with a supercritical conjugate condition followed by a hydraulic drop to the subcritical conditions in the counterflow region. Experimentally, no such jump–drop combinations have been observed. This has also been noted by Long (1970) under a different flow geometry.

(iii) $S_d \gtrless 1$, $h_1' < h_1$: The hydraulic jump becomes submerged or 'flooded' (Wilkinson & Wood, 1971). This has the effect of reducing the entrainment of ambient fluid into the buoyant jet.

(*b*) *Unstable discharge.* Discharge instability has been interpreted earlier as consisting of recirculation cells in the near-field with repeated entrainment of mixed water into the buoyant jet. This would lead to a continuous build-up of species concentration and buoyancy in the near-field. A steady-state limit on this build-up is reached when the stabilizing buoyant force has increased sufficiently to drive the counterflow system in balance with opposing inertial and frictional forces. In this limiting stage another critical section will be established at the edge of the near-field zone.

The mixing analysis for these cases is aimed at a single bulk property of the flow, namely the dilution ratio

$$S = \theta_0/\theta_1 = 2q_1/q_0, \tag{45}$$

in which θ_1 and q_2 are the species concentration and flow rate, respectively, for the upper layer of the counterflow region. For the stable discharge with cases (i) or (ii) this dilution is directly predicted from the buoyant jet flow up to the level of surface spreading, that is

$$S = q_t/q_0. \tag{46}$$

The submerged jump case (iii) presents considerable difficulties for dilution analysis due to the partial re-entrainment of mixed fluid leading to lower dilutions than given by (46). However, unless the receiving channel has a large dimension L, this case is of lesser importance and will be considered only as a transition between the stable discharge with normal jump and the unstable discharge cases.

4.2. *Stratified counterflow region*

The equations for the two-layered horizontal flow in the counterflow region are developed under the following approximations. (1) Hydrostatic pressure distribution. (2) Negligible turbulent entrainment across the interface. Since the flow solution of interest is subcritical, the bulk Richardson number condition derived by Ellison & Turner (1959) which governs vertical entrainment in horizontal shear flow will be satisfied. Thus, the discharge in each layer will be independent of x, q_1 = constant, q_2 = constant. (3) The vertical diffusion of the tracer is small compared to the horizontal tracer advection. This assumption is justifiable because of the sharp density change at the interface with small values of a local Richardson number (Turner 1973). Therefore the tracer and buoyancy flux in each layer is approximately constant. (4) The shear stresses at the channel surface, interface and bottom are τ_s, τ_i and τ_b, respectively, and will be related to the mean flow quantities. (5) Uniform profiles for the horizontal velocities u_1, u_2 and densities ρ_1, ρ_2 are assumed in each layer. Thus the significant governing equation is the horizontal momentum conservation equation (3) which can be integrated vertically over each layer to give (Schijf & Schonfeld 1953)

$$\frac{q_1^2}{gh_1^3}\frac{dh_1}{dx} = \frac{\rho_1}{\rho_2}\left(\frac{dh_1}{dx} + \frac{dh_2}{dx}\right) - \frac{\tau_s - \tau_i}{\rho_2 g h_1} \tag{47}$$

and

$$\frac{q_1^2}{gh_2^3}\frac{dh_2}{dx} = \frac{\rho_1}{\rho_2}\frac{dh_1}{dx} + \frac{dh_2}{dx} - \frac{\tau_i - \tau_b}{\rho_2 g h_2}, \tag{48}$$

where $\rho_2 = \rho_a$. Upon introduction of the Boussinesq approximation, (47) and (48) reduce to (Harleman 1960)

$$h_1 + h_2 = H, \tag{49}$$

i.e. constant total depth, and, with $\beta\theta_1 = (\rho_a - \rho_1)/\rho_a$,

$$\frac{dh_2}{dx} = \frac{1}{\rho_a \beta\theta_1 g(1 - F_1^2 - F_2^2)}\left[-\frac{\tau_s}{H - h_2} - \frac{\tau_b}{h_2} + \frac{\tau_i}{H - h_2} + \frac{\tau_i}{h_2}\right], \tag{50}$$

where F_1 and F_2 are as defined previously. Thus the slope of the interface is governed by a balance of buoyant and frictional forces. The shear stresses can be related to the mean flow quantities through the relationships (Bata 1957; Harleman 1960)

$$\tau_s = \tfrac{1}{8} f_s \rho_a u_1 |u_1|, \quad \tau_i = \tfrac{1}{8} f_i \rho_a (u_1 - u_2)\,|u_1 - u_2| \quad \text{and} \quad \tau_b = \tfrac{1}{8} f_b \rho_a u_2 |u_2| \tag{51}$$

in which f_s, f_i and f_b are the Darcy–Weisbach friction coefficients for surface, interface and bottom respectively which are independent of position x. (51) can be inserted into (50) and, at this point, the development will be restricted to equal counterflow, $q_1 = -q_2$, by virtue of large dilution ratios, so that

$$\frac{dh_2}{dx} = \frac{-f_s F_1^2 + f_b F_2^2 + f_i (F_1^{\frac{2}{3}} + F_2^{\frac{2}{3}})^3}{8(1 - F_1^2 - F_2^2)}. \tag{52}$$

Defining the non-dimensional variables $(h^*, x^*) = (h_2, x)/H$, the constant Froude number

$$F_H^2 = q_1^2 (\beta\theta_1 g H^3)^{-1} \tag{53}$$

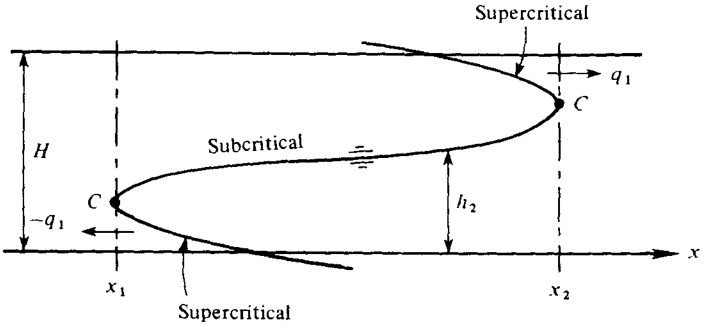

FIGURE 10. General shape of the interface equation (53) for equal counterflow. C indicates the critical depth.

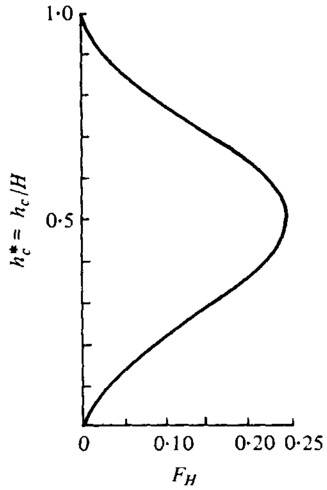

FIGURE 11. Critical depth in equal counterflow as a function of channel Froude number F_H.

and the ratios $\alpha_i = f_i/f_b$ and $\alpha_s = f_s/f_b$, (52) can be integrated to

$$x^* - x_1^* = \frac{8}{f_b F_H^2} \int_{h_1^*}^{h^*} \frac{h^{*3}(1-h^*)^3 - F_H^2[(1-h^*)^3 + h^{*3}]}{(1-h^*)^3 + \alpha_i - \alpha_s h^{*3}} \, dh^*, \tag{54}$$

where h_1^* represents a known depth at a given position x_1^* along the channel. The integral (54) is evaluated for a channel with a free surface $\tau_s = 0$ which is the geometry used in the present experiments. With the notation $\eta = 1 - h^*$, $a = \alpha_i^{\frac{1}{3}}$ and $c = \alpha_i + F_H^2$, (54) becomes

$$x^* - x_1^* = \frac{8}{f_b F_H^2} \left\{ \frac{(1-\eta)^4}{4} - a^3\eta + \frac{c + 3ac + a^6}{6a^2} \ln \frac{(\eta + a)^3}{\eta^3 + a^3} \right.$$
$$\left. + \frac{c - 3ac + a^6}{\sqrt{3}\, a^2} \tan^{-1} \frac{2-a}{a\sqrt{3}} + c \ln(\eta^3 + a^3) \right\}_{h_1^*}^{h^*}. \tag{55}$$

The general form of (55) is shown in figure 10 and consists of three branches which are divided by two critical sections where the interfacial slope goes to infinity. The subcritical branch is the important one in the present case. The critical depth h_c^* is

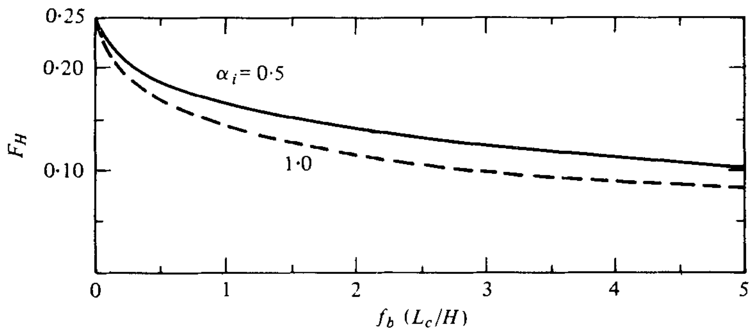

FIGURE 12. Relationship between channel Froude number F_H and far-field parameter $f_b L_c/H$ for different values of the resistance coefficient ratio $\alpha_i = f_i/f_b$.

obtained by setting the numerator under the integral sign in (54) equal to zero. The solution of the resulting equation (which is equivalent to (40)] is given in figure 11 as a function of the channel Froude number F_H. The solution is double-valued for $F_H < \frac{1}{4}$ which defines the subcritical domain. The higher value of h_c^* is the realistic one at the channel end as the mixed upper layer fluid undergoes a rapid depth change as it spreads into the outside reservoir. This solution can be taken as the boundary condition h_1^* at $x_1^* = L/H$ and (55) gives implicitly the interfacial height h^* as the function of channel position x^*. In particular, at the edge of the near-field $x_d^* = x_d/H$ the interfacial depth $\hat{h}_1$ is reached, which has been considered earlier for the stable discharge condition.

The length of the subcritical counterflow section $L_c/H = x_2^* - x_1^*$ is found for any $F_H < \frac{1}{4}$, if (55) is evaluated between two critical limits. The solution in terms of the parameter $f_b L_c/H$ is plotted in figure 12 for two values $\alpha_i = \frac{1}{2}$ and $\alpha_i = 1$. For unstable discharge conditions the counterflow length is related to the channel geometry as $L_c/H = L/H - 2{\cdot}5$ so that a unique Froude number F_H can be deduced from figure 12. The mixed flow in the upper layer is then given by virtue of (45) and (53) as

$$q_1 = \left(2\frac{I_1}{I_2}\right)^{\frac{1}{3}} F_H^{\frac{2}{3}} q_{\theta 0}^{\frac{1}{3}} H, \tag{56}$$

which is directly dependent on the initial buoyancy flux q_{θ_0} and the layer depth H. The prediction of the bulk dilution in the unstable discharge regime follows as

$$S = 4^{\frac{1}{3}} \left(\frac{F_H}{F_0}\right)^{\frac{2}{3}} \frac{H}{B}. \tag{57}$$

The value of the interfacial friction factor f_i has been a subject of several studies (Ippen & Harleman 1953; Bata 1957; Lofquist 1960; Abraham & Eysink 1971; Harleman & Stolzenbach 1972). These studies suggest that f_i is dependent on several factors, such as Reynolds number, internal Froude number, wall roughness and flow geometry. The data comparison by Harleman & Stolzenbach for stratified flows in which only one layer is moving suggests $f_i \approx f_b$, where f_b is the smooth-wall friction coefficient which can be estimated on the basis of flow Reynolds number. The lock exchange flow data, given by Abraham & Eysink, on the other hand, suggest $f_i \approx 0{\cdot}5 f_b$. Since that geometry is more similar to the counterflow condition in the present case, the later value is adopted here, so that $\alpha_i = \frac{1}{2}$.

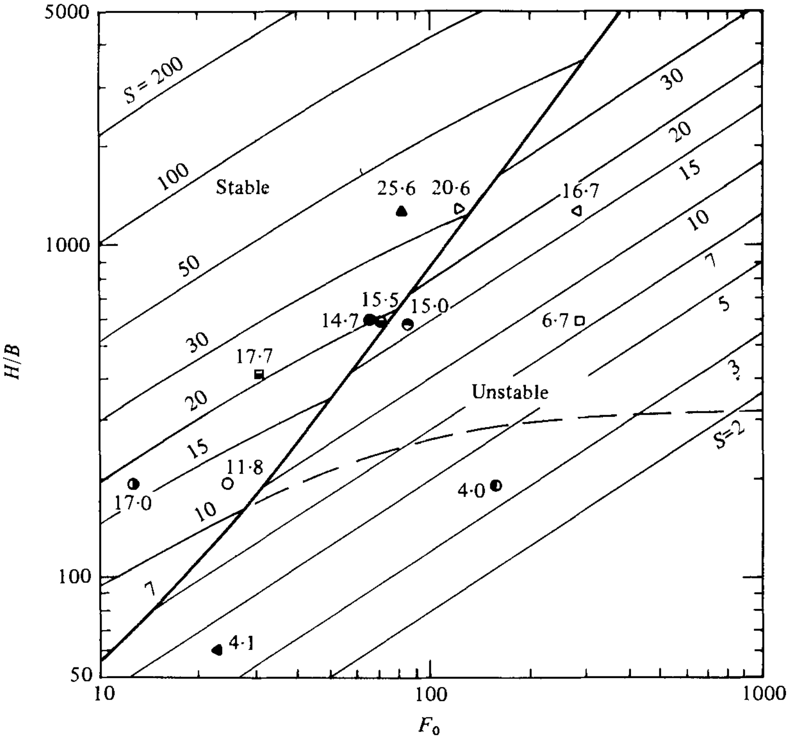

FIGURE 13. Dilution ratio S as a function of discharge conditions F_H and H/B and for $f_b L_c/H = 0{\cdot}5$. Experimental values include the range $0{\cdot}4 < f_b L_c/H < 0{\cdot}6$. The symbols and the flow fields to which they refer are given in table 1. The dashed line corresponds to dilution $S = 10$ predicted on the basis of buoyant jet theory alone without attention to recirculation effects.

4.3. *Dilution ratios*

The prediction of the dilution ratios for stable conditions (46) and for unstable conditions (57) is given in figure 13 for the F_0 and H/B parameter space. The Froude number in (54) has been evaluated with a far-field parameter value $f_b\, L_c/H = 0{\cdot}5$ which presents an average value for the experiments. The equal dilution lines do not match at the stability criterion. In practice, a smooth transition seems to be provided by a narrow region of submerged internal jump conditions which would decrease the dilution values at the edge of the stable discharge range below those predicted by simple buoyant jet theory (46). The dilution line $S = 10$ based on consideration of buoyant jet theory above without accounting for the effects of instability and recirculation has been shown as a dashed line in figure 13 in order to demonstrate the significantly lower mixing capability of unstable buoyant discharges. This has important implications on the design of environmental mixing devices as discussed in § 1.

5. Experiments

5.1. *Equipment and procedure*

The experiments were designed to study the mechanics of the plane vertical turbulent jet in confined depth over a wide range of the governing parameters: initial Froude number F_0, relative submergence H/B and far-field effects $f_b L_c/H$. The experiments (figure 2) were conducted in a relatively large flume – 15·3 m long, 1·4 m wide and 0·9 m deep – in order to ensure a high Reynolds number range through the flow field. The flume front wall had an observation window. The channel was formed by placing a plywood sheet of variable length at a distance of 30·5 cm from, and parallel to, the front wall of the flume. The flume was filled with water of laboratory ambient temperature with a variable depth H from 30 cm to 60 cm.

Heated water was injected through a chamber with flow distribution elements located at the midpoint of the channel and extending across the channel width. The chamber had a sliding plate on top which allowed the slot width B to be changed from 0·5 mm to 6·3 mm. The heated discharge flow was obtained via a steam heat exchanger, constant head tank and a calibrated flowmeter.

The temperature field was measured in two ways. First, thirty-six thermistor probes (YSI no. 401, time constant 7 s) were mounted in four vertical transects of nine probes each through the channel and fourteen more in the outside reservoir and in water supply lines. The probes were individually calibrated and were scanned by a high-speed scanning system. Second, a fast-response thermistor probe (Fenwall GA51SM2, time constant 0·07 s) was installed on a point gauge which was driven by a d.c. motor at a traversing speed of 0·7 cm s^{-1}. The point gauge itself was mounted on a movable carriage and could be moved at any position within the channel. The vertical probe position was recorded via a potentiometer and the probe voltage output via a Wheatstone bridge circuit on the two axes of an x–y plotter.

Injection of dye into the heated discharge allowed visual and photographic observation of the flow structure. In addition, limited measurements of the velocities were possible through time-lapse photographic recording of dye traces formed by falling dye crystals.

Before the start of an experiment an initial temperature scan was made to check the uniformity of temperature throughout the flume. At the start the heated water was turned on and an equal withdrawal flow was started. A slug of dye was injected into the initial discharge and the dye advance was observed. The flow had an initial unsteady phase, until the dye front reached the channel end, at which time the steady phase began. The steady state itself was limited in time owing to the finite reservoir volume outside. A gradual build-up of buoyant water in the reservoir resulted which ultimately exceeded the critical depth at the channel exit, so that backwater effects were felt in the channel. Depending on discharge conditions the initial unsteady portion varied between 5 and 10 minutes and the steady phase between 15 and 30 minutes. Measurements were taken in the steady phase and showed a time-independent behaviour of the flow and temperature field.

Experiment	H (cm)	B (mm)	U_0 (cm s^{-1})	L (m)	θ_0 (°C)	R_j	L/H	$\hat{f}_b$	$\frac{f_b L_c}{H}$	F_0	H/B	Observed flow field	S (Observed)	S (Theory)	Symbol
1	61·0	3·2	19·5	6·1	8·5	1610	10	0·066	0·50	25	192	Stable	11·8	12·2	○
2	61·0	3·2	13·1	6·1	16·1	1070	10	0·066	0·50	13	192	Stable	17·0	17·0	◑
3	61·0	3·2	130·2	6·1	9·1	10700	10	0·054	0·41	160	192	Unstable	4·0	3·5	◐
4	61·0	1·0	52·5	6·1	13·4	1370	10	0·065	0·49	87	600	Unstable	15·0	16·1	◓
5	61·0	1·0	26·8	6·1	6·1	700	10	0·071	0·53	71	600	Stable	15·5	19·0	◒
6	61·0	1·0	46·1	6·1	16·4	1200	10	0·060	0·45	67	600	Stable	14·7	19·2	●
7	61·0	1·0	143·7	6·1	9·7	3750	10	0·061	0·46	291	600	Unstable	6·7	7·3	□
8	40·6	1·0	82·1	6·1	12·2	2140	15	0·058	0·73	144	400	Unstable	7·3	7·3	◨
9	30·5	1·6	56·7	6·1	9·9	2330	20	0·061	1·07	91	192	Unstable	5·1	4·6	◧
10	30·5	1·6	162·9	6·1	9·4	6700	20	0·055	0·96	270	192	Unstable	2·5	2·3	⬒
11	66·2	1·6	19·5	6·1	13·8	810	9	0·068	0·44	31	416	Stable	17·7	21·0	⬓
12	61·0	3·2	65·0	6·1	8·9	5350	10	0·047	0·35	80	192	Unstable	5·5	5·7	△
13	38·1	6·4	32·6	6·1	11·7	5360	16	0·052	0·70	23	60	Unstable	4·1	3·8	▽
14	66·2	0·5	40·0	6·1	8·0	540	9	0·070	0·46	128	1300	Stable	20·6	28·0	▷
15	66·2	0·5	119·6	6·1	12·8	1610	9	0·063	0·41	293	1300	Unstable	16·7	15·9	◁
16	66·2	0·5	39·7	6·1	15·8	540	9	0·068	0·44	85	1300	Stable	25·6	36·0	▲
17	61·0	3·2	56·7	3·7	8·6	4760	6	0·060	0·21	70	192	Unstable	6·7	6·5	▼
18	61·0	1·0	143·7	3·7	8·4	3750	6	0·061	0·21	312	600	Unstable	7·5	7·4	▶
19	38·1	6·4	32·6	3·7	11·9	5360	10	0·052	0·39	23	60	Unstable	4·1	4·1	◀

TABLE 1. Listing of experimental parameters and results.

5.2. *Comparison of theory and experiments*

Nineteen experiments covering the range, F_0 from 13 to 312, H/B from 60 to 1300, $f_b L_c/H$ from 0·21 to 1·07, were performed with the vertical buoyant jet. The exact conditions, governing parameters and observed results for each experiment are listed in table 1.

Two parameters in table 1 deserve comment as they affect the comparison between experiment and theory. The jet Reynolds number is defined as $R_j = 4U_0 R_h/\nu$, where R_h is the hydraulic radius and ν the kinematic viscosity. For the slot discharge $R_h = \frac{1}{2}B$. No exact dependence of the jet entrainment as a function of R_j is known, in particular for slot discharges. Pearce (1968) made visual observations of round non-buoyant jets with diameter D, so that $R_h = \frac{1}{4}D$, over a wide R_j range. He found laminar behaviour with only minor instabilities for $R_j < 500$, fully turbulent conditions for $R_j > 3000$ and a transition in between.

Further exploratory studies in the transition range by Ungate, Jirka & Harleman (1975) for round jets with and without buoyancy seem to indicate a critical value of $R_{jc} \sim 1200$ to 1500 above which the jet mixing appears to be independent of R_j. Decreasing values of dilution, however, were found for $R_j < R_{jc}$ in particular for buoyant jets. Assuming a similar behaviour for slot jets it can be expected that those experiments with $R_j < 1200$ to 1500 may have lower dilutions than predicted by theory. With the experimental procedure, using heated water as the buoyancy source, it was not possible to avoid this limitation.

Although the theory was developed for an ideal two-dimensional flow field, the experiments were subject to lateral wall friction. While this effect can be expected to be insignificant in the near-field, it will influence the behaviour of the stratified counterflow in the far-field. The following approximate procedure has been used to account for this effect. Inclusion of the wall stress $2\tau_{W_1}$ on both walls bounding the upper layer in (47) and of $2\tau_{W_2}$ for the lower layer in (48) leads to the following correction factors for f_i and f_b in (52):

$$c_i = 1 + \frac{f_w}{4f_i}\frac{H}{W} \quad \text{and} \quad c_b = 1 + \frac{f_w}{f_b + 4f_i}\frac{H}{W}, \tag{58}$$

where f_w is the Darcy–Weisbach friction coefficient for the wall boundary and W the channel width. An equal layer depth $h_1 \approx h_2$ has been assumed in (58) so that c_i and c_b are approximately constant along the channel. Thus the corrected values are $\hat{f}_b = c_b f_b$ and $\hat{f}_i = c_i f_i$. The ratio $\hat{\alpha}_i = \hat{f}_i/\hat{f}_b$, however, is largely unaffected by the wall shear as $c_i/c_b \approx 1$ for the present geometry, so that $\hat{\alpha}_i \approx \alpha_i$, which is taken as $\frac{1}{2}$ as mentioned in §4.2. The values of f_b and $\hat{f}_w$ were estimated from a White–Colebrook friction diagram based on the predicted Reynolds number in the counterflow region $R = q_1/\nu$ and for a smooth wall boundary. The parameter $f_b L_c/H$ listed in table 1 reflects this procedure.

Examples of the observed two-dimensional temperature field for stable and unstable discharge conditions are shown in figure 14(*a*) and 14(*b*), respectively. In all experiments the flow structure was similar on both sides of the symmetry line $x = 0$ so that only the region $x > 0$ is shown. The normalized excess temperature θ/θ_0 is plotted for different vertical profiles along the channel. Both vertical and horizontal distances are normalized, z/H and x/H. Separate investigations show temperature uniformity in the third co-ordinate direction across the channel. The following properties can be inferred from figure 14 in agreement with the theoretical development.

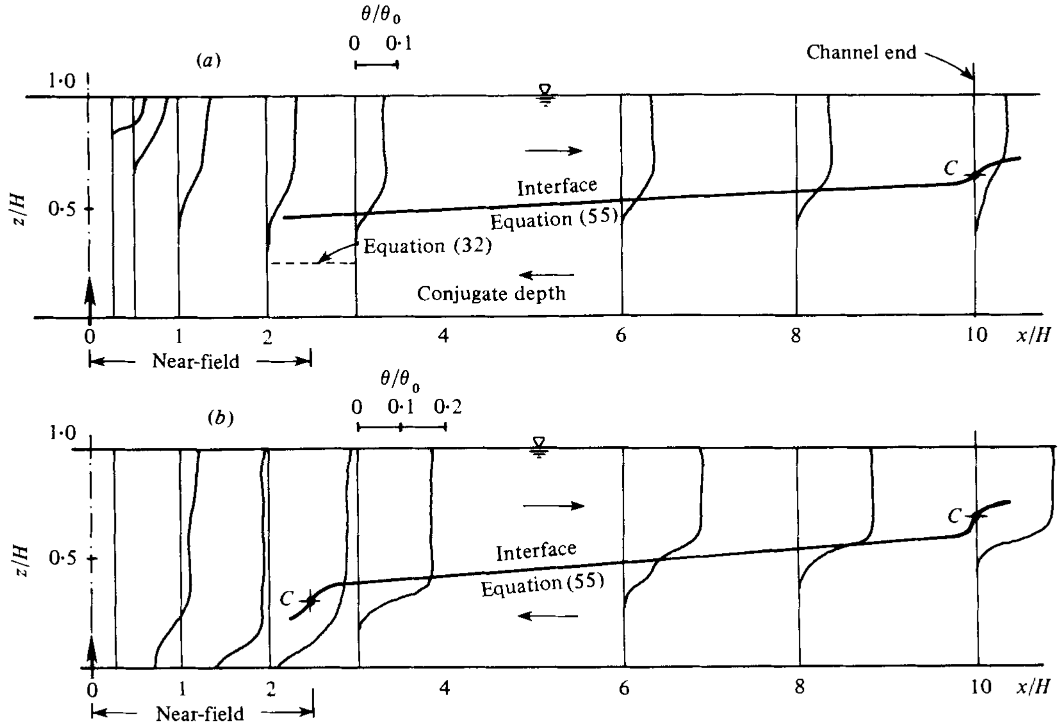

FIGURE 14. Measured temperature field for stable and unstable discharge configuration, respectively. Comparison with theoretical predictions (55) of interface position in counter flow region. C indicates critical depth. (*a*) Experiment 6, stable near-field. (*b*) Experiment 12, unstable near-field.

(*a*) *Stable discharge* (figure 14*a*). The impingement layer thickness is in the order $h_1/H \sim \frac{1}{6}$ and shows a relatively uniform temperature distribution. In the hydraulic jump zone, $0{\cdot}25 < x/H < 2{\cdot}5$, a rapid increase in layer thickness occurs. There is no significant temperature change along the jump indicating minimal entrainment from the lower layer. The temperature distribution in the stratified counterflow region, $x/H > 2{\cdot}5$, shows strong density interfaces and horizontal and vertical uniformities in each layer. Thus there is negligible mixing across the interface and negligible heat loss to the laboratory environment, confirming the assumption of a conservative tracer. A rapid upper layer depth change occurs at the channel end indicating a critical depth transition. The same features can be seen in figure 3 (*c*) which corresponds qualitatively to figure 14 (*a*). Theoretical predictions of layer depth in the hydraulic jump and counterflow regions are also included in figure 14 (*a*) and show excellent agreement with the observations. Condition (i) governs the near- and far-field interaction as discussed in §4.1.

(*b*) *Unstable discharge* (figure 14*b*). The near-field recirculation cell shows a relatively uniform temperature distribution except for a thin layer close to the bottom in which the ambient water which enters the recirculation zone is still incompletely mixed. The critical section at the edge of the near-field $x/H \sim 2{\cdot}5$ is characterized by a rapid change in layer depth. The counterflow region has similar features to those in the stable discharge mode, including another critical section at the channel end.

Figure 4(*c*) shows similar characteristics as the temperature plot, figure 14(*b*). The observed interfacial shape of the counterflow region is in good correspondence with the theoretical prediction using (55).

The observations on discharge stability are compared in figure 9 with the theoretical criterion (44). In the experiments, the discharge was defined as unstable (*a*) on the basis of visual dye observation and (*b*) when a temperature rise was observed at the bottom boundary of the near-field zone (see figure 14*b*). Both definitions always concurred. The excellent agreement in figure 9 suggests the accuracy of the theory for the behaviour of buoyant jets in confined depth.

The experimental dilution ratio S was calculated from (45) on the basis of the observed temperature rise θ_1 in the counterflow region. The experimental values are listed in table 1 along with the theoretical ones. Except for low observed values for several experiments in the stable discharge range the values are in good agreement. The assumptions made in the theory were examined for the source of this discrepancy. Only two factors can be singled out. First, and probably as the major cause, it appears that the dilution of those experiments is influenced by low jet Reynolds numbers R_j. In fact, close inspection of table 1 suggests some correlation of R_j with the ratio of observed dilution to predicted dilution. In particular experiments 14 and 16 with the lowest $R_j = 540$ shows the lowest ratio, i.e. an observed dilution about 23 % lower than the theoretical. For increasing R_j, the theoretical and experimental values approach each other. The critical value R_{jc} appears to be in the range of 1200 to 1500, as has been discussed earlier on the basis of round jet investigations. Secondly, the stable experiments with F_0 and H/B values close to the instability range can possibly experience some effects of submerged hydraulic jump and the associated entrainment of mixed water into the buoyant jet. This possibility has been mentioned in §4.3 and can be seen better by plotting the experimental values into a dilution diagram covering the F_0 and H/B range. This has been done in figure 13 for those experiments with the far-field parameter $f_b L_c/H$ in the range from 0·4 to 0·6 which approximate the theoretical value 0·5 which forms the basis of figure 13 in the unstable range.

The mixing characteristics of the unstable discharge mode are controlled by the boundary and interfacial friction of the far-field, represented by $f_b L_c/H$ and $\alpha_i = f_i/f_b$. This dependence is demonstrated by plotting in figure 15 the factor $SF_0^{\frac{2}{3}}(H/B)^{-1}$ as a function of $f_b L_c/H$, where the theoretical values of S are obtained from (57). The experimental values show a definite decreasing trend for increasing $f_b L_c/H$ and agree well with the theoretical predictions for $\alpha_i = 0{\cdot}5$. This supports the choice of Abraham & Eysink's (1971) data base for the estimation of interfacial friction in counterflow situations.

6. Concluding remarks

This study has been concerned with the stability and mixing characteristics of plane turbulent buoyant jets discharging vertically into a receiving medium of confined depth. It has been demonstrated that discharge stability is purely dependent on the near-field behaviour of the jet, that is the dynamic interaction of the buoyant jet region, the surface impingement region and the internal hydraulic jump region. The stability is independent of the far-field geometry of the receiving medium. Stable discharge configurations then have a buoyant jet region which is decoupled from the

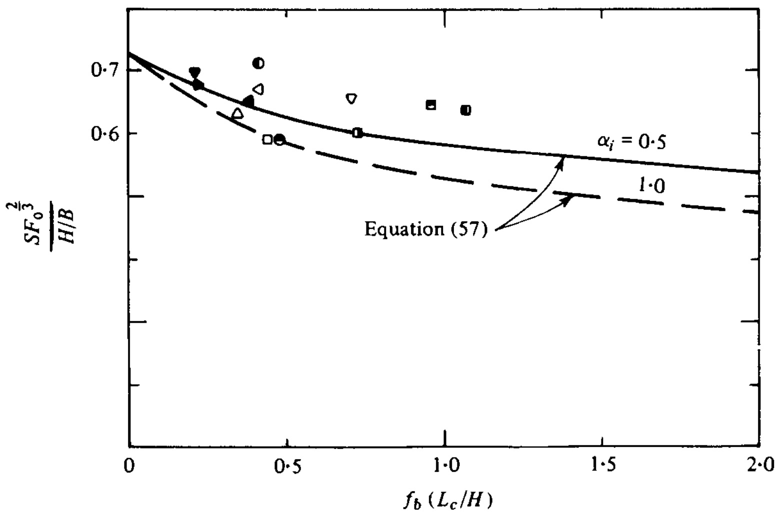

FIGURE 15. Comparison of normalized dilution $SF_0^{\frac{2}{3}}(H/B)^{-1}$ for theory and experiment as a function of far-field parameter $f_b L_c/H$. Symbols are identified in table 1.

horizontal spreading motion along the free surface of the medium. Unstable discharge configurations, on the other hand, are distinguished by vertical recirculation cells leading to re-entrainment of mixed fluid into the jet proper. A criterion for discharge stability has been defined in terms of two governing parameters, a discharge densimetric Froude number and a relative submergence. This criterion can be used to classify buoyant discharges in diverse engineering applications, such as injections into mixing chambers, fire plumes, disposal of effluents into the ocean and atmosphere, and others.

The far-field geometry of the receiving medium has a significant influence on the bulk mixing characteristics of the discharge. This is especially important for unstable discharges in which the continuous build-up of species concentrations in the recirculation process is limited by the buoyancy-driven convection in the far-field. In the present study, a far-field geometry was assumed which ensures a steady-state flow field and mixing characteristics. The geometry consists of a finite length channel which contains the buoyant discharge at its midpoint and which communicates with a large outside reservoir. A critical section exists at the channel end and provides a virtual control on the flow field. Geometries of this type with characteristic horizontal lengths can be identified in several practical applications, for example the corridor length in case of fire plumes or the diffuser pipe length for effluent discharges.

It is interesting to consider alternate far-field geometries and their effect on discharge mixing. (i) For an infinitely long channel a density current will progress in the channel and will experience an increasing frictional resistance. This can be expected to lead to a concentration build-up over time. This unsteady behaviour, in fact, constitutes the initial phase in the present experiments as was described in §5.1. (ii) If the receiving medium is contained in a box of finite length, then a gradual displacement of ambient fluid with mixed fluid will take place, leading to concentration increases over time. This situation resembles the model by Baines & Turner (1969), although they did not consider the question of near-field stability in their analysis.

The success of the present study in predicting a complex flow phenomenon suggests extensions to other discharge configurations, such as axisymmetric jets and non-vertical injections.

REFERENCES

ABRAHAM, G. 1963 Jet diffusion in stagnant ambient fluid. *Delft Hydr. Lab. Publ.* no. 29.

ABRAHAM, G. 1965 Entrainment principle and its restriction to solve jet problems. *J. Hydraul. Res., I.A.H.R.* **31**, 1–23.

ABRAHAM, G. & EYSINK, W. D. 1971 Magnitude of interfacial shear in exchange flow. *J. Hydr. Res. I.A.H.R.* **9**, 125–151.

ABRAHAM, G. & JIRKA, G. H. 1974 Discussion of 'Turbulent entrainment on buoyant jets and plumes', *J. Hydraul. Div., Proc. A.S.C.E.* **100** (HY8), 1180–1181.

ABRAMOVICH, G. W. 1963 *The Theory of Turbulent Jets.* The M.I.T. Press.

ALBERTSON, M. L., DAI, Y. B., JENSEN, R. A. & ROUSE, H. 1950 Diffusion of submerged jets. *Trans. A.S.C.E.* **115**, 639–664.

BAINES, W. D. & TURNER, J. S. 1969 Turbulent buoyant convection from a source in a confined region. *J. Fluid Mech.* **37**, 51–80.

BATA, G. L. 1957 Recirculation of cooling water in rivers and canals. *J. Hydraul. Div., Proc. A.S.C.E.* **83** (HY3), 1265, 1–27.

BRADSHAW, P. 1977 Effect of external disturbances on the spreading rate of a plane turbulent jet. *J. Fluid Mech.* **80**, 795–797.

COLA, R. 1966 Diffusione di un getto piano verticale in un bacino d'acqua d'altezza limitata. *L'Energia Elettrica* **43**, 1–19.

CHU, V. H. & VANVARI, M. R. 1976 Experimental study of turbulent stratified shearing flow. *J. Hydraul. Div., Proc. A.S.C.E.* **102** (HY6), 691–706.

ELLISON, T. H. & TURNER, J. S. 1959 Turbulent entrainment in stratified flows. *J. Fluid Mech.* **6**, 423–448.

HARLEMAN, D. R. F. 1960 Stratified flow. In *Handbook of Fluid Dynamics* (ed. V. L. Streeter). McGraw-Hill.

HARLEMAN, D. R. F. & STOLZENBACH, K. D. 1972 Fluid mechanics of heat disposal from power generation. *Ann. Rev. Fluid Mech.* **4**, 7–32.

IAMANDI, C. & ROUSE, H. 1969 Jet-induced circulation and diffusion, *J. Hydraul. Div., Proc. A.S.C.E.* **95** (HY2), 589–601.

IPPEN, A. T. & HARLEMAN, D. R. F. 1951 Steady-state characteristics of subsurface flow. *Nat. Bur. Stand. Circ.* no. 521.

ITO, H. 1960 Pressure losses in smooth pipe bends. *J. Basic Engng Trans. A.S.M.E.* **82**, 131–143.

JIRKA, G. H., ABRAHAM, G. & HARLEMAN, D. R. F. 1975 An assessment of techniques for hydrothermal prediction. *M.I.T. Parsons Lab. for Water Resour. & Hydrodyn., Rep.* 203.

KOH, R. C. Y. 1971 Two-dimensional surface warm jet. *J. Hydraul. Div., Proc. A.S.C.E.* **97** (HY6), 819–836.

KOH, R. C. Y. & BROOKS, N. H. 1975 Fluid mechanics of waste water disposal in the ocean. *Ann. Rev. Fluid Mech.* **7**, 187–211.

KOTSOVINOS, N. E. 1976 A note on the spreading rate and virtual origin of a plane turbulent jet. *J. Fluid Mech.* **77**, 305–311.

KOTSOVINOS, N. E. & LIST, E. J. 1977 Plane turbulent jets. Part 1. Integral properties. *J. Fluid Mech.* **81**, 25–44.

LEE, S. L. & EMMONS, H. W. 1961 A study of thermal convection above a line fire. *J. Fluid Mech.* **11**, 353–368.

LIST, E. J. & IMBERGER, J. 1973 Turbulent entrainment in buoyant jets and plumes. *J. Hydraul. Div., Proc. A.S.C.E.* **99** (HY9), 1461–1474.

LIST, E. J. & IMBERGER, J. 1975 Closure of discussion to 'Turbulent entrainment in buoyant jets and plumes'. *J. Hydraul. Div., Proc. A.S.C.E.* **101** (HY5), 617–620.

LOFQUIST, J. 1960 Flow and stress near an interface between stratified liquids. *Phys. Fluids* **3**, 158–175.

LONG, R. R. 1970 Blocking effects in flows over obstacles. *Tellus* **22**, 471–480.

LONG, R. R. 1972 Finite amplitude disturbances in the flow of inviscid rotating and stratified fluids over obstacles. *Ann. Rev. Fluid Mech.* **4**, 69–92.

MEHROTRA, S. C. 1973 Limitations on the existence of shock solutions in a two-fluid system. *Tellus* **25**, 169–173.

MEHROTRA, S. C. 1976 Length of hydraulic jump. *J. Hydraul. Div., Proc. A.S.C.E.* **102** (HY7), 1027–1033.

MEHROTRA, S. C. & KELLY, R. E. 1973 On the question of non-uniqueness of internal hydraulic jumps and drops in a two-fluid system. *Tellus* **25**, 560–567.

MORTON, B. R. 1959 Forced plumes. *J. Fluid Mech.* **5**, 151–163.

MORTON, B., TAYLOR, G. I. & TURNER, J. S. 1956 Turbulent gravitational convection from maintained and instantaneous sources. *Proc. Roy. Soc.* A **234**, 1–23.

MUROTA, A. & MURAOKA, K. 1967 Turbulent diffusion of a vertically upward jet. *Proc. 12th Cong. I.A.H.R., Colorado*, vol. 4, pp. 60–70.

PAN, F. & ACRIVOS, A. 1967 Steady flows in rectangular cavities. *J. Fluid Mech.* **28**, 643–655.

PEARCE, A. F. 1966 Critical Reynolds number for fully developed turbulence in circular submerged water jets. *Counc. Scientific Ind. Res. South Africa, Rep.* no. MEG 475.

PRIESTLEY, C. H. B. & BALL, F. K. 1955 Continuous convection from an isolated source of heat. *Quart. J. Roy. Met. Soc.* **81**, 144–157.

ROUSE, H., YIH, C.-S. & HUMPHREYS, H. W. 1952 Gravitational convection from a boundary source. *Tellus* **4**, 201–210.

SCHIJF, J. B. & SCHONFELD, J. C. 1953 Theoretical considerations on the motion of salt and fresh water. *Proc. Minnesota Int. Hydraul. Convention, I.A.H.R. & A.S.C.E.* 321–328.

SCHLICHTING, H. 1968 *Boundary Layer Theory.* McGraw-Hill.

SCHMIDT, F. H. 1957 On the diffusion of heated jets. *Tellus* **9**, 378–383.

SCHMIDT, W. 1941 Turbulente Ausbreitung eines Stromes erhitzter Luft. *Z. angew. Math. Mech.* **21**, 358–363.

TOLLMIEN, W. 1926 Die Berechnung turbulenter Ausbreitungsvorgange. *Z. angew. Math. Mech.*, **6**, 468–478.

TURNER, J. S. 1973 *Buoyancy Effects in Fluids.* Cambridge University Press.

UNGATE, C. D., JIRKA, G. H. & HARLEMAN, D. R. F. 1975 Mixing of submerged turbulent jets at low Reynolds numbers. *M.I.T. Parsons Lab. for Water Resour. & Hydrodyn., Rep.* no. **197**.

Van der Hegge Zijnen, B. G. 1958 Measurements of the distribution of heat and matter in a plane turbulent jet of air. *Appl. Sci. Res.* **7**, 277–292.

WILKINSON, D. L. & WOOD, I. R. 1971 A rapidly varied flow phenomenon in a two-layer flow. *J. Fluid Mech.* **47**, 241–256.

YIH, C.-S. 1965 *Dynamics of Nonhomogeneous Fluids.* The MacMillan Co.

YIH, C.-S. & GUHA, C. R. 1955 Hydraulic jump in a fluid system of two layers. *Tellus* **7**, 358–366.

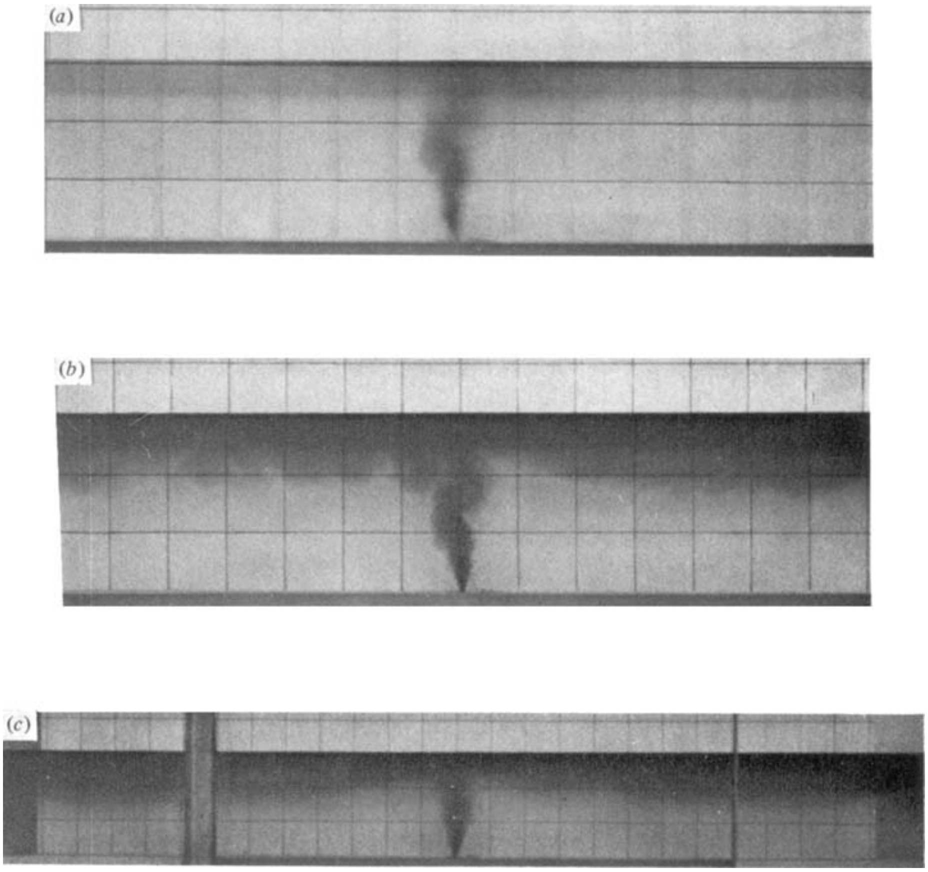

FIGURE 3. Flow visualization of stable discharge configuration by means of continuous dye injection under steady-state heated discharge conditions ($U_0 = 25{\cdot}9$ cm s^{-1}, $B = 1{\cdot}6$ mm, $\theta_0 = 23{\cdot}3$ °C, $H = 30$ cm). Grid size 10 × 10 cm. (*a*) Dye pattern at 10 s after start of dye injection. (*b*) Dye pattern at 40 s. (*c*) Steady-state dye pattern over complete channel length.

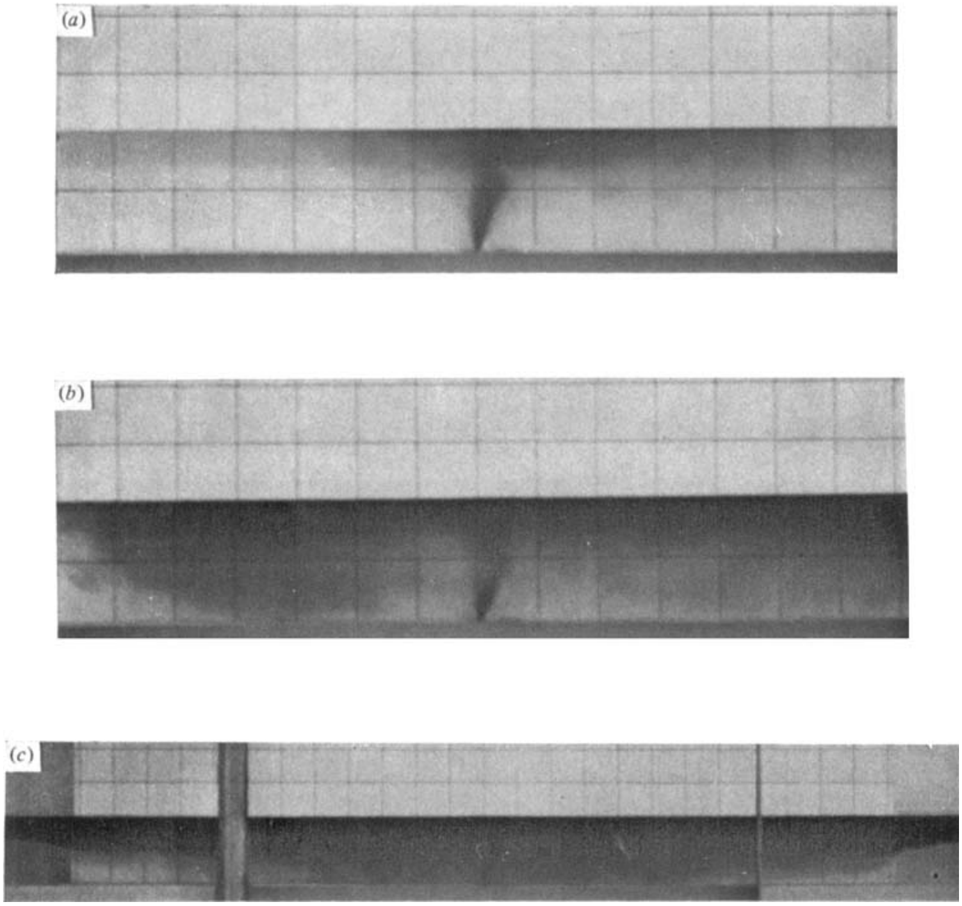

FIGURE 4. Flow visualization of unstable discharge configuration by means of continuous dye injection under steady-state heated discharge conditions ($U_0 = 53{\cdot}7$ cm s^{-1}, $B = 1{\cdot}6$ mm, $\theta_0 = 8{\cdot}3$ °C, $H = 20$ cm). Grid size 10×10 cm. (*a*) Dye pattern at 10 s after start of injection. (*b*) Dye pattern at 40 s. (*c*) Steady-state dye pattern over complete channel length.

JIRKA AND HARLEMAN